

New constraints on the central mass contents of Omega Centauri from combined stellar kinematics and pulsar timing

Andrés Bañares-Hernández^{1,2*}, Francesca Calore³, Jorge Martin Camalich^{1,2,4}, and Justin I. Read⁵

¹ Instituto de Astrofísica de Canarias, La Laguna, Tenerife, E-38200, Spain

² Departamento de Astrofísica, Universidad de La Laguna

³ CNRS, Laboratoire d'Annecy-le-Vieux de Physique Théorique, 74940, Annecy, France

⁴ CERN, Theoretical Physics Department, CH-1211 Geneva 23, Switzerland

⁵ Department of Physics, University of Surrey, Guildford, GU2 7XH, United Kingdom

August 27, 2024

ABSTRACT

Aims. We perform a combined analysis of stellar kinematics with line-of-sight accelerations of millisecond pulsars (MSPs) to probe the mass contents of Omega Centauri (ω Cen). Our mass model includes the stellar mass distribution, a more concentrated mass component linked to the observed MSP population, a generic cluster of stellar remnants (assumed to be more concentrated than the stars and MSPs), and an intermediate-mass black hole (IMBH), allowing us to determine which of these is most favored.

Methods. We mass-model ω Cen using the package GravSphere to solve the Jeans equations, including constraints from proper motions, line-of-sight velocities, the surface density profile of the stars, the spatial distribution of MSPs, and the recently measured line-of-sight accelerations of a subset of these MSPs, self-consistently modeling their intrinsic spin-down. We explore the impact of different assumed centers of ω Cen on our results and we infer the posterior distributions of the model parameters from the combined likelihood using the nested sampling package dynesty.

Results. Our analysis favors an extended central mass of $\sim 2 - 3 \times 10^5 M_{\odot}$ over an IMBH, setting a 3σ upper limit on the IMBH mass of $6 \times 10^3 M_{\odot}$. We find that pulsar timing observations are an important additional constraint, favoring a central mass distribution that is $\sim 20\%$ more massive and extended than for models that are constrained by the stellar kinematics alone. Finally, we find a 3σ CL upper bound of $6 \times 10^4 M_{\odot}$ on the total mass traced by the MSPs, with the density profile following $\rho_p(r) \propto \rho_{\star}(r)^{\gamma}/\sigma(r)$, with $\gamma = 1.9 \pm 0.3$, where $\rho_{\star}(r)$ is the stellar mass density and $\sigma(r)$ is the stellar velocity dispersion profile. This favors models in which MSPs form via stellar encounters, such as the leading paradigm whereby MSPs are the progeny of low-mass X-ray binaries.

Conclusions. Our analysis demonstrates how combining stellar kinematics with MSP accelerations produces new constraints on mass models, shedding light on the presence or absence of IMBHs at the centers of globular clusters. Further, we provide the first validation of its kind where MSP positions are linked to their place of formation in globular clusters, showing excellent agreement with the expectation of stellar encounter models of MSP formation. This sets a promising precedent amid the advent of the rapidly growing number of observations and discoveries currently being experienced in this field.

Key words. galaxy / globular clusters: individual: Omega Centauri, stars / pulsars: general, stars: black holes, stars: kinematics and dynamics, galaxies: kinematics and dynamics, galaxies / star clusters: general, cosmology: dark matter

1. Introduction

The origin and structure of Omega Centauri (ω Cen) is a highly debated topic. Being the most massive and luminous globular cluster (GC) in the Milky Way, it has been argued that ω Cen may not be strictly speaking a GC, but rather the remnant core of a tidally disrupted, nucleated, dwarf galaxy (Bekki & Freeman 2003; Wirth et al. 2020; Johnson et al. 2020). Evidence in favor of this hypothesis includes the observation of a retrograde orbit (Dinescu et al. 1999), which may be associated with the disruption of the so-called “Sequoia” (Myeong et al. 2019) or Gaia-Enceladus galaxies (Massari et al. 2019), the detection of a long tidal stream (Ibata et al. 2019), and a new formation mechanism for nucleated dwarfs that was recently proposed by Gray et al. (2024). In their model, the smallest nucleated dwarfs have their star formation first quenched by reionization and then reignited in a major-merger driven starburst. The dense nucleus forms in this starburst, yielding a galaxy with two distinct stellar populations that have a large age gap. This observational feature has

been seen in several massive Milky Way GCs, including ω Cen (Gray et al. 2024).

Recent numerical simulations from Wirth et al. (2020) suggest that, if ω Cen is indeed an accreted nucleated dwarf, then it can retain significant amounts of dark matter even as it tidally disrupts. By performing a Jeans analysis of stellar kinematics, Brown et al. (2019) and Evans et al. (2022) found that the presence of an extended dark component in ω Cen is statistically favored, and that dark matter self-annihilation could account for the observation of γ -ray signals. However, millisecond pulsars (MSPs) are known γ -ray emitters and can also account for the observed γ -ray emission (Reynoso-Cordova et al. 2021; Dai et al. 2023, 2020).

Alongside the possible presence of dark matter, ω Cen is interesting as a possible location for the formation of black hole seeds via runaway stellar collisions (e.g. Portegies Zwart et al. 2004) or the formation and death of a supermassive star (e.g. Chon & Omukai 2020). Several authors (Noyola et al. 2008; Noyola et al. 2010; Jalali et al. 2012; Baumgardt 2017) found evidence of a $\sim 3 - 5 \times 10^4 M_{\odot}$ intermediate-mass black hole

* a.banareshernandez@gmail.com

(IMBH) at the center of ω Cen from the consideration of stellar kinematic data (using either Jeans models or N-body simulations). However, [Van der Marel & Anderson \(2010\)](#), via a Jeans-based analysis, derived a 3σ upper bound on the IMBH mass of $1.8 \times 10^4 M_\odot$, in tension with the previously cited masses. [Baumgardt et al. \(2019\)](#) also found no evidence of an IMBH by comparing N-body simulations to data for ω Cen (stellar velocity dispersion, surface brightness, and proper motion data), favoring instead a centrally concentrated cluster of stellar-mass black holes that accounts for 4.6% of the mass of ω Cen. [Zocchi et al. \(2017\)](#) and [Zocchi et al. \(2019\)](#) stress that the presence of an IMBH in ω Cen can be degenerate with orbital anisotropy and with the presence of a cluster of mass-segregated stellar-mass black holes. [Evans et al. \(2022\)](#) concluded that a core of stellar remnants can account for up to $\sim 5 \times 10^5 M_\odot$ of the inner dark mass derived in their analysis, with a dark matter also being a potential explanation. Therefore, the structure and composition of the mass content of ω Cen remains a subject of ongoing debate.

In recent years, MSP timing observations have been used to probe the gravitational potential and mass contents of GCs, with a growing wealth of data being produced¹ and analyzed in this context ([Prager et al. 2017](#); [Freire et al. 2017](#); [Perera et al. 2017a,b](#); [Kızıltan et al. 2017a,b](#); [Abbate et al. 2018](#); [Abbate et al. 2019](#); [Xie & Wang 2020](#); [Ridolfi et al. 2021](#); [Wang & Xie 2021](#); [Zhang et al. 2023](#); [Dai et al. 2023](#); [Padmanabh et al. 2024](#); [Xie et al. 2024](#); [Vleeschower et al. 2024](#)). We also refer the interested reader to earlier studies where this methodology was explored, such as in [Phinney \(1993\)](#) and [Anderson \(1993\)](#).

In [Dai et al. \(2023\)](#), constraints on accelerations from five centrally located (with projected radii within a few pc from the center) MSPs in ω Cen were measured via Doppler-induced effects in timing observations from the pulsars discovered in [Dai et al. \(2020\)](#). [Dai et al. \(2023\)](#) reported a tension between the extremal bounds derived from the baryonic profile used to model the mass content of ω Cen and the comparatively high inferred pulsar accelerations. This opens the possibility for MSP line-of-sight (LOS) accelerations to play a role in understanding the structure of ω Cen, adding to the previous discussion. In particular, robust constraints on accelerations near the central region could allow one to discern between the various profiles postulated with unprecedented accuracy, with the ability to identify sufficiently centrally concentrated distributions should they be present.

With the above in mind, in this work we carry out a Jeans-based analysis exploiting velocity dispersion (proper motion and line-of-sight) and surface brightness profile data with an implementation based on the publicly available code GravSphere² ([Read & Steger 2017](#); [Read et al. 2018](#); [Genina et al. 2020](#); [Collins et al. 2021](#)). At the same time, we also include novel constraints on both the pulsar distribution and line-of-sight acceleration data from [Dai et al. \(2023\)](#) as a self-consistent modification to the original likelihood function used in GravSphere. This allows us to fully exploit both the stellar and MSP timing-derived kinematics.³

¹ For an updated census of observed MSPs in GCs, we refer the interested reader to this convenient web resource by P.C.C. Freire: <https://www3.mpifr-bonn.mpg.de/staff/pfreire/GCpsr.html>

² <https://github.com/justinread/gravsphere>

³ We note that during the preparation of this manuscript we were made aware of a recent parallel study that builds on work in [Hénault-Brunet et al. \(2020\)](#) to also combine stellar kinematics with pulsar accelerations to improve mass models ([Smith et al. 2024](#)). Their approach is complementary to ours. They also include both stellar kinematic constraints and pulsar accelerations in a similar joint likelihood function, but they

An additional novel feature of our approach is that we decompose the inner mass distribution within ω Cen into a potential IMBH and an additional population tracing the observed distribution of MSPs. This allows us to break degeneracies between the mass in remnants and the possible presence of an IMBH, as well as giving us a robust constraint on the spatial distribution of MSPs. This latter can also be used to shed light on the origin of the gamma-ray emission observed in ω Cen ([Brown et al. \(2019\)](#); [Reynoso-Cordova et al. \(2021\)](#); [Dai et al. \(2023, 2020\)](#)).

This paper is organized as follows. In Sec. 2, we describe the mass modeling method that we use in this work and the treatment of the stellar kinematics. In Sec. 3, we discuss the stellar photometric and kinematic data we use. In Sec. 4, we discuss the pulsar timing data that we use to determine the pulsar accelerations, while in Sec. 5 we address their implementation in our methodology. In Secs. 6 - 8, we present our key results and we discuss them in the context of previous studies in the literature of ω Cen. Finally, in Sec. 9 we present our conclusions.

2. Jeans modeling of stellar kinematics

Our mass modeling method is adapted from the Jeans equations solver GravSphere. We start with a brief overview of how the latest version of GravSphere works. A more detailed discussion can be found in [Read & Steger \(2017\)](#); [Genina et al. \(2020\)](#); [Collins et al. \(2021\)](#) and [Júlio et al. \(2023\)](#).

In essence, GravSphere is designed to solve the Jeans equations under the assumption of a non-rotating, spherically symmetric stellar system which is in a steady state. This can be used to map velocity dispersion and surface brightness profile of collisionless tracer particles, such as stars in self-gravitating objects like galaxies and GCs, to the total underlying mass distribution.

We start by considering the dynamical equation governing the phase-space distribution function $f(\mathbf{x}, \mathbf{v}, t)$ of a collisionless system of particles, e.g. stars, given by the collisionless Boltzmann equation:

$$\frac{df}{dt} = \frac{\partial f}{\partial t} + \nabla_{\mathbf{x}} f \cdot \mathbf{v} - \nabla_{\mathbf{v}} f \cdot \nabla_{\mathbf{x}} \Phi = 0, \quad (1)$$

where Φ is the gravitational potential resulting from all mass components in the system, and satisfying the Poisson equation:

$$\nabla_{\mathbf{x}}^2 \Phi = 4\pi G \rho, \quad (2)$$

where ρ is the total mass density of the system.

Although the distribution function f is normally not directly accessible via observations, one can multiply Eq. (1) by powers of the velocity components and integrate in velocity space to arrive at a dynamic equation in terms of velocity moments which do relate to observable properties (e.g. see [Binney & Tremaine \(2008\)](#); [Battaglia et al. \(2013\)](#)). In particular, taking the steady state solution $\frac{\partial f}{\partial t} = 0$ for the first moment and multiplying by each velocity component v_j , one obtains a set of three well-known equations: The Jeans equations ([Jeans 1922](#)), which can be expressed as:

$$\sum_{i=1}^3 \frac{\partial v_{\star} \langle v_i v_j \rangle}{\partial x_i} + v_{\star} \frac{\partial \Phi}{\partial x_j} = 0, \quad (3)$$

implement this within the distribution function modeling code Limepy ([Gieles & Zocchi 2015](#)). They then apply their method to the 47 Tuc and Terzan 5 GCs, whereas we focus here on ω Cen.

where $v_*(\mathbf{x}) = \int d^3v f$ is the stellar (tracer particle) number density and $\langle v_i v_j \rangle = \int d^3v v_i v_j f$ correspond to the two-point velocity moments, with the brackets “ $\langle \rangle$ ” generally denoting an integral with the distribution function over velocity space.

For the case of a spherically symmetric distribution, one finds that the only non-trivial equation becomes that involving the radial component, which can be expressed in terms of the radial / tangential velocity dispersions (respectively):

$$\sigma_{r/t}^2 = \langle v_{r/t}^2 \rangle - \langle v_{r/t} \rangle^2 \quad (4)$$

to give the spherical Jeans equation:

$$\frac{1}{v_*} \frac{\partial v_* \sigma_r^2}{\partial r} + \frac{2\beta \sigma_r^2}{r} = -\frac{GM}{r^2}, \quad (5)$$

where

$$\beta \equiv 1 - \frac{\sigma_t^2}{\sigma_r^2} \quad (6)$$

is the so-called velocity anisotropy⁴ and we adopt a Newtonian potential with enclosed mass $M(r)$ within the 3D radial coordinate r . It should also be understood that $v_*, \beta, \sigma_r, \sigma_t$ are all, in general, functions of r .

Eq. (5) can be solved for the quantity $v_* \sigma_r^2$ yielding the radial velocity dispersion (Mamon & Łokas 2005; van der Marel 1994):

$$\sigma_r^2(r) = \frac{1}{v_*(r)g(r)} \int_r^\infty \frac{GM(r')v_*(r')}{r'^2} g(r') dr', \quad (7)$$

where

$$g(r) \equiv \exp\left(2 \int \frac{\beta(r)}{r} dr\right). \quad (8)$$

The LOS projection of σ_r^2 , which is a commonly used observable (e.g. Strigari et al. (2007)), is then given by (Binney & Mamon 1982)

$$\sigma_{\text{Los}}^2(R) = \frac{2}{\Sigma_*(R)} \int_R^\infty \left(1 - \frac{R^2}{r^2} \beta(r)\right) \frac{v_*(r) \sigma_r^2(r) r}{\sqrt{r^2 - R^2}} dr, \quad (9)$$

where $\Sigma_*(R)$ corresponds to the stellar surface density at a projected radius R , and one multiplies by the geometrical factors corresponding to the contributions of the radial and tangential components along the line of sight, taking a density-weighted average along the line of sight.

Having discussed some of the basic elements of a Jeans analysis, we now address an issue which arises due to the fact that (even if the photometric profiles of Σ_*, v_* are well constrained from surface brightness data) there is a clear degeneracy between the anisotropy β and the enclosed mass $M(r)$ in Eqs. (7,9). This is known as the M - β degeneracy (or also, by extension, the ρ - β degeneracy, where $\rho(r)$ is the density) and has been extensively discussed in the literature (Merrifield & Kent 1990; Wilkinson et al. 2002; Łokas & Mamon 2003; de Lorenzi et al. 2009; Read & Steger 2017). This problem is a manifestation of the fact that the Jeans equations alone are not a closed system, meaning that they cannot unambiguously constrain these two quantities without more information being provided.

⁴ Note that here we use the 1D tangential velocity dispersion. Some authors use the 2D tangential velocity dispersion, in which case the second term in Eq. (6) should be divided by a factor of two.

Following, for example, Watkins et al. (2013); Van der Marel & Anderson (2010), in order to resolve the mass-anisotropy degeneracy, one can obtain expressions for the projected proper motions along the projected radius R and the tangential component (respectively), these are given by:

$$\sigma_{\text{PM},R}^2(R) = \frac{2}{\Sigma_*(R)} \int_R^\infty \left(1 - \beta(r) + \frac{R^2}{r^2} \beta(r)\right) \frac{v_*(r) \sigma_r^2(r) r}{\sqrt{r^2 - R^2}} dr \quad (10)$$

and

$$\sigma_{\text{PM},t}^2(R) = \frac{2}{\Sigma_*(R)} \int_R^\infty \left(1 - \beta(r)\right) \frac{v_*(r) \sigma_r^2(r) r}{\sqrt{r^2 - R^2}} dr. \quad (11)$$

Furthermore, following Merrifield & Kent (1990); Richardson & Fairbairn (2014), to help eliminate the ρ - β degeneracy, one can integrate with higher moments of velocity in the collisionless Boltzmann equation, Eq. (1), to obtain two independent observables known as virial shape parameters (VSPs), which are given by

$$\text{VSP1} = \frac{2}{5} \int_0^\infty GMv_*(5 - 2\beta) \sigma_r^2 r dr = \int_0^\infty \Sigma_* \langle v_{\text{LOS}}^4 \rangle R dR \quad (12)$$

and

$$\text{VSP2} = \frac{4}{35} \int_0^\infty GMv_*(7 - 6\beta) \sigma_r^2 r^3 dr = \int_0^\infty \Sigma_* \langle v_{\text{LOS}}^4 \rangle R^3 dR, \quad (13)$$

where one can obtain data from observations corresponding to the RHS of Eqs. (12) and (13) that can therefore constrain β .

For the photometric tracer density profile, in this paper, we introduce the generic $\alpha\beta\gamma$ profile, which has been used in a variety of contexts (Hernquist 1990; Zhao 1996; Di Cintio et al. 2014; Freundlich et al. 2020; Zentner et al. 2022) due to its ability to reproduce a diverse range of distributions analytically. This is given by a double power-law model given as follows:

$$v_*(r) = \frac{\rho_c}{(r/r_c)^\gamma (1 + (r/r_c)^\alpha)^{(\gamma-\beta)/\alpha}}, \quad (14)$$

where we have introduced the three exponent variables α, β, γ , and the scale radius and density r_c, ρ_c , respectively. In previous versions of GravSphere, a summation of mass components given by Plummer sphere profiles (Plummer 1911) was used. Plummer models are commonly used in this context and have been found to provide adequate fits to photometric profiles in many cases, while having a simple analytical form. However, we found the model we used was able to reproduce the observed surface brightness profile significantly better, particularly at larger projected radii where the profile becomes shallower than what Plummer-based models allow.

The projected tracer surface density, is then given by:

$$\Sigma_*(R) = \int_{-\infty}^\infty v_*(r(l)) dl, \quad (15)$$

where, for carrying out the integral, l corresponds to the coordinate along the LOS so that $r(l) = \sqrt{R^2 + l^2}$. Unlike the original version of GravSphere, to aid computational efficiency, we precompute this projection before fitting the kinematic and acceleration data, thereby assuming that the uncertainty on the photometric light profile is small as compared to the uncertainty on the velocity dispersion profiles. We explicitly checked that this is a good approximation for ω Cen.

To obtain the corresponding (cumulative) mass profile $M_\star(r)$, one can simply integrate Eq. (14) over space and multiply by a normalization factor needed to match the total mass of the distribution M_\star . This factor corresponds to the mass-to-light ratio (if using luminosities rather than number densities or arbitrary units for the surface density profile), which is assumed to be constant throughout the profile.

For the full mass modeling, besides the photometric mass profile $M_\star(r)$, which accounts for the dynamical mass of the photometric distribution, including stars and any remnants or objects traced by this distribution, we add a central mass, $M_{\text{cen}}(r)$, which emulates a generic central cluster of remnants. This central mass is modeled as a single Plummer sphere component (Plummer 1911) given by

$$M_{\text{cen}}(r) = M_{\text{cen}} \frac{r^3}{r_{\text{cen}}^3} \left(1 + \frac{r^2}{r_{\text{cen}}^2} \right)^{-3/2}, \quad (16)$$

where in this case we introduce the corresponding total mass and scale lengths M_{cen} and r_{cen} , respectively. To model the presence of an IMBH, we also introduce a point mass M_{BH} .

Lastly, since the full likelihood implementation of MSP data requires a model of the MSP distribution (see Sec. 5.2), we also include a mass component that follows the MSP profile. This allows us to consider the presence of a distribution of stellar remnants traced by the MSPs that are more centrally concentrated than the stars. This profile is given by

$$M_p(r) = \frac{4M_p}{3\sqrt{\pi}} \frac{\Gamma[(1-\alpha)/2]}{\Gamma[-(\alpha/2+1)]} \frac{r^3}{r_0^3} {}_2F_1 \left[\frac{3}{2}, \frac{1-\alpha}{2}; \frac{5}{2}; -\frac{r^2}{r_0^2} \right], \quad (17)$$

where ${}_2F_1$ is the Gaussian hypergeometric function and M_p is the total mass of the distribution, which is defined (convergent) for the density exponent parameter $\alpha < -2$, while r_0 is the length scale parameter. This equation is obtained by integrating the density with the functional form shown in Eq. (30) over space and multiplying it by the normalization factor to obtain the mass distribution. The resulting total mass profile is thus given by:

$$M(r) = M_\star(r) + M_{\text{cen}}(r) + M_{\text{BH}} + M_p(r). \quad (18)$$

While dark remnant models of ω Cen favor two-component profiles of light and heavy remnants (see discussion in Sec. 8.2), in general, different populations of objects are expected to show different degrees of segregation based on their dynamical histories and their intrinsic masses. Being more massive than main-sequence stars, but less than heavy remnants (such as stellar-mass black holes), MSPs could indeed trace a distribution of intermediate concentration, should the system undergo sufficient mass segregation (e.g. Phinney (1993)). There is also no a priori reason to exclude the coexistence of an IMBH with a central remnant distribution, which is an important consideration given that both have been invoked to explain ω Cen's kinematics. Therefore, to fully explore all these scenarios, their potential kinematic relevance, and to explicitly consider any potential degeneracies between them, we have decided to work with the generic multi-component model from Eq. (18).

We use the anisotropy profile assumed in GravSphere following the generalized form from Baes & van Hese (2007), which is an extension of the Osipkov-Merritt anisotropy profile (Osipkov 1979; Merritt 1985), and is given by

$$\beta(r) = \beta_0 + (\beta_\infty - \beta_0) \frac{1}{1 + \left(\frac{r}{r_t}\right)^\eta}, \quad (19)$$

where β_0 is the anisotropy at the center, β_∞ its limit as it asymptotically approaches infinity, r_t is the transition scale between these two regimes, and η is the exponent which modulates the steepness of the transition.

3. Stellar kinematic and photometric data

We combine the LOS stellar kinematic data from Reijns et al. (2006) with Sollima et al. (2009), adjusting their individual line of sight velocities to match the value in Pechetti et al. (2024), $\langle v_{\text{LOS}} \rangle = 232.5$ km/s. This accounts for any systematic offset between the different datasets (the shift is of order 1 km/s, which is smaller than the uncertainty on the individual stellar velocities). We perform a quality cut on these data, retaining only those stars with velocity error smaller than 4 km/s. This yields 1644 LOS velocities. We augment these with the Noyola et al. (2010) data that are pre-binned for three different choices of center; more on this, below. We take HST proper motion (PM) data from Bellini et al. (2017), augmenting this with Gaia proper motion data from Vasiliev & Baumgardt (2021). As with the LOS data, we perform a similar quality cut on the PM data, retaining stars with PM uncertainties smaller than 2 km/s at the distance of ω Cen (assumed to be 5.2 kpc; see Sec. 4). The PM data are perspective corrected as in van de Ven et al. (2006), assuming a mean LOS velocity and distance, as above. The surface brightness data are taken from the Bellini et al. (2017) catalog and augmented with Gaia photometry from de Boer et al. (2019). We explore three different choices of center for ω Cen taken from Anderson & Van der Marel (2010) (RA, DEC = 201.69683333, -47.47956944), Noyola et al. (2008) (RA, DEC = 201.69184583, -47.47911111) and the kinematic center from Noyola et al. (2010) (RA, DEC = 201.69630208, -47.47835389). These centers are self-consistently computed for the photometric light profile, LOS and PM stellar kinematic data.

The LOS velocity and PM data are then binned using the `binulator`, as described in Collins et al. (2021). We use 100 logarithmically spaced bins, ensuring that no bin has less than 100 stars in it. For the LOS data, we augment the post-binned data with the pre-binned data from Noyola et al. (2010), using the consistent center reported in that work. `binulator` calculates the two virial shape parameters, VSP1 and VSP2 (see Sec. 8.1) and their uncertainties. As such, we use these also in our fits to assist with breaking the mass-anisotropy degeneracy (see Sec. 2). We explicitly checked whether our choices of binning parameters impact our results. Replacing our binned PM data with the binned data from Watkins et al. (2015a) yielded similar results for our mass components, with the main difference being a somewhat more extended distribution for the central mass component, which had a comparable total mass, showing no significant differences for the IMBH component. The stellar kinematic data and the best-fit photometric parameters used in this study have been made publicly available.⁵

4. Pulsar timing observations

Although pulsars are known to be remarkably regular sources, over sufficiently long time scales, it is in fact possible to detect significant variations in the observed period of these objects. This effect encodes information on the relative acceleration between the observer and pulsar reference frames, as well as the

⁵ <https://github.com/dadams42/OcenKinematics>

intrinsic spin-down of the pulsar (e.g. see [Phinney \(1993\)](#)), and can be calculated through the following equation:

$$\left(\frac{\dot{P}}{P}\right)_{\text{obs}} = \frac{a_{\text{LOS}} + a_S + a_g}{c} + \left(\frac{\dot{P}}{P}\right)_{\text{int}}, \quad (20)$$

where c is the speed of light and $P_{\text{obs/int}}$, $\dot{P}_{\text{obs/int}}$ denote the period and its time derivative in the observer / pulsar rest frames (respectively), with the second term in the RHS corresponding to the intrinsic spin-down contribution of the pulsar. The first term in the RHS accounts for the various contributions due to the relative motions between the pulsar and the observer which induce an effective time-dependent Doppler shift in the observed period. We will now address the various components which constitute this term.

a_g is the relative difference in LOS accelerations due to the differential Galactic rotations of the GC and the Solar System. Following [Dai et al. \(2023\)](#); [Freire et al. \(2017\)](#) and Section 5.1.2 of [Prager et al. \(2017\)](#), we use Equation 5 from [Nice & Taylor \(1995\)](#) yielding

$$a_g = -\cos(b) \left(\frac{\Theta_0^2}{R_0}\right) \left(\cos(l) + \frac{\beta}{\sin^2(l) + \beta^2}\right) \text{ m s}^{-2}, \quad (21)$$

where $\beta = (d/R_0)\cos(b) - \cos(l)$. $R_0 = 8.34 \pm 0.16$ kpc is the distance from the Sun to the Galactic center and $\Theta_0 = 240 \pm 8$ km/s is the Galactic rotational speed at that point, both of which are obtained from [Reid et al. \(2014\)](#). The distance from the cluster is fixed to $d = 5.2$ kpc. This value was originally chosen for consistency with the values reported in [Bellini et al. \(2014\)](#); [Watkins et al. \(2015a,b\)](#), and was subsequently validated throughout our analysis (see Sec. 8.1). We use the Galactic coordinates $\ell = 309.1^\circ$, $b = 14.97^\circ$ corresponding to the center of ω Cen located at RA = 13:26:47.24, DEC = -47:28:46.5 adopted in [Dai et al. \(2023\)](#).⁶

For the propagation of errors, we used the 68% confidence limit (CL) interval about the median obtained after running one million iterations, where a set of random samples is generated for the input parameters Θ_0, R_0 , under the assumption that they are independent and normally distributed with median values and errors as cited.

a_S accounts for the proper motion of the GC which induces an apparent LOS acceleration contribution – the Shklovskii effect – which is given by ([Shklovskii 1970](#); [Dai et al. 2023](#))

$$a_S = 3.78 \times 10^{-12} \left(\frac{d}{5.2 \text{ kpc}}\right) \left(\frac{\mu_T}{\text{mas yr}^{-1}}\right)^2 \text{ m s}^{-2}, \quad (22)$$

where $\mu_T = \sqrt{\mu_\delta^2 + \mu_{\alpha^*}^2}$ is the proper motion, and we take $\mu_\delta = -6.7445 \pm 0.0019$ mas yr⁻¹, $\mu_{\alpha^*} = -3.1925 \pm 0.0022$ mas yr⁻¹ ([Helmi et al. 2018](#)).

a_{LOS} corresponds to the LOS component of the acceleration caused by the gravitational field of the GC on the pulsar and, under the assumption of spherical symmetry, is given by

$$a_{\text{LOS}}(r, l) = -G \left(\frac{l}{r}\right) \frac{M(r)}{r^2}, \quad (23)$$

⁶ This center was originally reported in [Harris \(1996\)](#) catalog (2010 edition). It is essentially equivalent to the [Anderson & Van der Marel \(2010\)](#) center, which is the main center we adopt and present in this analysis for the stellar kinematic and photometric data. For the remaining centers (Appendix C), given the relatively extended positions of the MSPs and that these are not dependent on binning prescriptions, the choice of center should have a limited effect on the results obtained.

where l in this case is the longitudinal component (i.e. along the line of sight) of the position of the pulsar from the center of the GC and r is the total distance, so that $r = \sqrt{l^2 + R^2}$, where R is the projection orthogonal to the line of sight and is typically the one that can be measured directly. $M(r)$ denotes the enclosed mass of the spherical density distribution, while the geometric factor l/r projects the LOS component of the total radial acceleration experienced by the pulsar. This is the component of the observed period derivative which traces the mass contents of the GC, and is therefore the reason why these timing observations are of interest for the present study.

While the intrinsic spin-down component is subject to significant uncertainties and is difficult to measure directly, it can, however, be approximated to a model of magnetic dipole emission with braking index $n = 3$, yielding ([Prager et al. 2017](#); [Dai et al. 2023](#))

$$a_{\text{int}} \equiv c \left(\frac{\dot{P}}{P}\right)_{\text{int}} \approx 7.96 \times 10^{-10} \left(\frac{B}{2 \times 10^8 \text{ G}}\right)^2 \left(\frac{2 \text{ ms}}{P_{\text{obs}}}\right)^2 \text{ m s}^{-2}, \quad (24)$$

where B is the surface magnetic field strength of the pulsar, whose effective values can be constrained from observations where this term is dominant (see Sec. 5.3).

5. Likelihood definition

5.1. Implementation of stellar kinematics constraints

For the purposes of fitting the stellar kinematics observables discussed in Sec. 2, one can construct a general log-likelihood function for the proper motion and LOS velocity dispersions, and the virial shape parameters, taking the form:

$$\ln \mathcal{L}(\theta) = -\frac{1}{2} \sum_y \chi_y^2, \quad (25)$$

where we have the general chi-square variable for an observable y defined as

$$\chi_y^2 \equiv \sum_i \frac{[y_{i, \text{obs}} - y_i(\theta)]^2}{\delta y_i^2}, \quad (26)$$

and observables are taken to be normally distributed with median values $\{y_{i, \text{obs}}\}$ and corresponding standard errors $\{\delta y_i\}$, and $\{y_i(\theta)\}$ correspond to the predicted variables as a function of the mass and (symmetrized) anisotropy model parameters θ .

5.2. Implementation of pulsar constraints

There are various possible ways to implement the pulsar timing constraints. However, there are some subtleties that should be considered when doing so. For example, a pointwise optimization for each of the pulsars over the nuisance parameter l can be quite numerically expensive if this has to be done for each step of a fitting routine. Also, errors or confidence intervals in acceleration constraints are not originally given in [Dai et al. \(2023\)](#) and can be difficult to quantify, particularly when including the intrinsic spin-down contribution.

To allow for an effective implementation and with the above discussion in mind, we include in the fit the quantity:

$$a_{\text{obs}} \equiv c \left(\frac{\dot{P}}{P}\right)_{\text{obs}} - a_g - a_S = a_{\text{LOS}} + c \left(\frac{\dot{P}}{P}\right)_{\text{int}}, \quad (27)$$

where the RHS follows directly from Eq. (20) and corresponds to the theoretical prediction from the GC mass model used, including the contribution from the intrinsic spin-down in Eq. (24). This observable is well constrained in each of its components. The errors can be propagated following our approach in Sec. 4: We simulate one million samples assuming that input variables are independent and normally distributed, with the specified errors and median values taken from the literature (see Sec. 4). We checked explicitly that the resulting distributions of a_{obs} were close to normal and obtained similar values to those predicted by common standard error propagation techniques (i.e. applying the central limit theorem to linear expansions of the functions). The resulting median values and errors on a_{obs} , as well as some of the data of the MSPs published in Dai et al. (2023), are shown in Table 1.

The term to be added to the log-likelihood function takes the form:

$$\ln \mathcal{L}_{p, \text{LOS}}(\theta_M; \{l_i\}, \{B_i\}) = -\frac{1}{2} \sum_i^{N_p} \frac{(a_{\text{obs},i} - a(\theta_M; l_i, B_i))^2}{\delta a_i^2}, \quad (28)$$

where $a(\theta_M; l_i, B_i)$ is the predicted LOS acceleration including intrinsic spin-down (RHS of Eq. (27)) and θ_M are the set of parameters characterizing the mass model. The parameters $\{B_i\}$ and $\{l_i\}$ correspond to the (unknown) magnetic field and longitudinal components of each of the N_p pulsars (5 in our case) while $\{\delta a_i\}$ are the propagated errors of Table 1.

To perform the fit, we marginalize over the parameters $\{B_i\}$ and $\{l_i\}$. The l_i are allowed to vary over a wide range within the boundaries of the GC. The reason B is marginalized over is that it has not been measured for this sample of MSPs. However, a reasonable idea of its range can be obtained based on known measurements performed on similar MSP populations. This is possible by measuring period variations for MSPs with no GC potential contributions, meaning that, after correcting for differential Galactic rotation and the Shklovskii effect, these observations act as direct tracers of the intrinsic spin-down contributions. For binary systems that do not experience significant orbital variability, Doppler-induced changes can also be studied in orbital period derivatives, with the added benefit of being independent of intrinsic spin-down effects (e.g. Freire et al. (2017); Prager et al. (2017)). To date, of the 18 known MSPs discovered in ω Cen, only the 5 used in this study have measured spin period derivatives and the only known binary from this set has not had its orbital period derivative measured (Dai et al. 2023). Therefore, we resort to existing studies of comparable MSP populations to constrain the intrinsic spin-down components. In particular, Prager et al. (2017) found using data from spin-dominated MSP populations in the ATNF catalog (Manchester et al. 2005) that the inferred distribution of B was well approximated to be log-normal with median $\log_{10} B$ [G] = 8.47 and standard deviation of 0.33 dex, which we adopt as a prior. This allows for an ample range which captures some of the uncertainty in the intrinsic spin-down, while also being representative of the values expected for MSP populations.

a_{obs} can be regarded as a strict upper bound on the acceleration, in the sense that the contribution due to intrinsic spin-down will always be negative. This translates to a lower bound on the enclosed mass when the accelerations are negative. Implementing this as a prior during the fits would be a somewhat simpler approach and has the advantage of not depending on the uncertainties in the intrinsic spin-down. However, it is likely less constraining and would require the potentially numerically expen-

sive pointwise optimization over the nuisance parameters $\{l_i\}$ to determine whether the bound is satisfied.

To fully exploit the MSP data and help further constrain parameters, we adopt an approach similar to the one used by Prager et al. (2017) and Abbate et al. (2018). We add a positional component to the likelihood function, adopting the ‘‘generalized King model’’ profile which is typically used to model MSP populations. This has a surface density given by (Lugger et al. 1995):

$$n(R) = n_0 \left[1 + \left(\frac{R}{r_0} \right)^2 \right]^{\alpha/2}, \quad (29)$$

where we have two additional free parameters: the exponent α , which modulates the steepness of the distribution; and the scale radius r_0 . (We also have the additional parameter n_0 , which is the central surface density. However, this is not included in the fit as it is a global factor and the likelihood components that we shall introduce are independent of it.)

As seen in Grindlay et al. (2002), the 3D density has the form:

$$n(r) = f(\alpha, r_0, n_0) \left[1 + \left(\frac{r}{r_0} \right)^2 \right]^{(\alpha-1)/2}, \quad (30)$$

where $f(\alpha, r_0, n_0)$ is a normalization factor that can be determined using the relation of the projected surface density (as in Eq. (15)) so that

$$n(R) = \int_{-\infty}^{\infty} n \left(\sqrt{R^2 + l^2} \right) dl, \quad (31)$$

and one can verify that this expression yields Eq. (29) with

$$f(\alpha, r_0, n_0) = \frac{\Gamma[(1-\alpha)/2] n_0}{\sqrt{\pi} \Gamma(-\alpha/2) r_0}, \quad (32)$$

where Γ denotes the Euler gamma function.

To quantify the positional probability to be added to the likelihood function, we follow a similar approach to Appendix D of Anderson (1993) and Phinney (1993); Prager et al. (2017); Abbate et al. (2018). We express the total positional probability density (for an individual pulsar) as:

$$P(l, R|\alpha, r_0) = P(l|R, \alpha, r_0)P(R|\alpha, r_0), \quad (33)$$

where:

$$\begin{aligned} P(l|R, \alpha, r_0) dl &= \frac{n \left(\sqrt{R^2 + l^2} \right) dl}{\int_{-\infty}^{\infty} n \left(\sqrt{R^2 + l'^2} \right) dl'} \\ &= \frac{\Gamma[(1-\alpha)/2] n_0}{\sqrt{\pi} \Gamma(-\alpha/2) r_0} \frac{1 \left[1 + (R^2 + l^2)/r_0^2 \right]^{(\alpha-1)/2}}{\left[1 + (R/r_0)^2 \right]^{\alpha/2}} dl, \end{aligned} \quad (34)$$

and:⁷

$$\begin{aligned} P(R|\alpha, r_0) dR &= \frac{R n(R) dR}{\int_0^{\infty} R' n(R') dR'} \\ &= -(\alpha+2) \frac{R}{r_0^2} \left[1 + \left(\frac{R}{r_0} \right)^2 \right]^{\alpha/2} dR, \end{aligned} \quad (35)$$

⁷ Note that, in our definition, R is non-negative, so that we only integrate from 0 outwards. (Extending this to negative values would only change the integral by a global factor of 2 which would not affect our results.)

Table 1. Data from MSPs published in Dai et al. (2023) with the inclusion of our derived median values and 68% CL errors of a_{obs} , as defined in Eq. (27), as well as the central values of R (see discussion following Eq. (23) for details).

Name	P_{obs} [ms]	\dot{P}_{obs} [10^{-20} s s $^{-1}$]	RA [J2000]	DEC [J2000]	R [pc]	a_{obs} [10^{-9} m s $^{-2}$]
J1326-4728A	4.108786192190(1)	2.738(2)	13:26:39.6699(2)	-47:30:11.641(3)	2.89	1.914 ± 0.011
J1326-4728B	4.791869161014(2)	-5.433(4)	13:26:49.5688(3)	-47:29:24.889(4)	1.14	-3.483 ± 0.011
J1326-4728C	6.867859692327(6)	0.98(1)	13:26:55.2219(6)	-47:30:11.753(9)	2.96	0.344 ± 0.012
J1326-4728D	4.578833468410(2)	-4.110(4)	13:26:32.7130(2)	-47:28:40.053(3)	3.72	-2.775 ± 0.012
J1326-4728E	4.2077170407405(4)	1.628(1)	13:26:42.67844(7)	-47:27:23.999(1)	2.38	1.076 ± 0.011

Notes. Error propagation follows the approach outlined in Sec. 4.

where in Eq. (34) we divide the infinitesimal amount of pulsars expected in a 3D ring of radius R , width dR , and length dl by those in the infinite cylinder of equal radius and width, recovering Eq. (3.7) of Phinney (1993). Similarly, for Eq. (35) we do the 2D analog, with the surface element of an annulus of width dR and radius R , integrating the whole disk with the projected surface density to obtain the relevant normalization factor in the denominator.

The complete positional probability for N_p pulsars is thus given by:

$$P(l, R|\alpha, r_0) = -\frac{\alpha + 2}{\sqrt{\pi}} \frac{\Gamma[(1 - \alpha)/2]}{\Gamma[-\alpha/2]} \frac{R}{r_0^3} \left[1 + (l^2 + R^2)/r_0^2 \right]^{(\alpha-1)/2}, \quad (36)$$

yielding the relevant (i.e., non-constant) contribution to the log-likelihood function:

$$\begin{aligned} \ln \mathcal{L}_{\text{pos}}(\{l_i\}, \alpha, r_0) &= \frac{\alpha - 1}{2} \sum_i^{N_p} \ln(1 + (R_i^2 + l_i^2)/r_0^2) \\ &+ N_p \left(\ln \frac{\Gamma[(1 - \alpha)/2]}{\Gamma[-\alpha/2]} + \ln[-(\alpha + 2)] - 3 \ln r_0 \right). \end{aligned} \quad (37)$$

Since Chen et al. (2023) have also reported the positions of 13 additional MSPs, but without the relevant timing data that trace kinematics, one can still use these positions to constrain the MSP distribution without the need to introduce any additional free parameters. For this purpose, we focus only on the projected radius component of the likelihood (as l becomes a redundant parameter). This gives the following log-likelihood:

$$\begin{aligned} \ln \mathcal{L}_{\text{pos, R}}(\alpha, r_0) &= \frac{\alpha}{2} \sum_i^{N_p} \ln \left[1 + \left(\frac{R_i}{r_0} \right)^2 \right] \\ &+ N_p (\ln[-(\alpha + 2)] - 2 \ln r_0). \end{aligned} \quad (38)$$

Note that in our treatment of the likelihood implementation of these MSP observables we have been careful to include normalization factors that depend on the parameters α and r_0 . While these are not always explicitly shown in previous works (and can sometimes be ignored), they are necessary to include whenever they are parameter-dependent and not merely global factors of the likelihood or, correspondingly, additive constants in the log-likelihood function.

Table 2. Priors implemented in dynesty for our analysis.

Parameter	Units	Prior Type	Range
$\tilde{\beta}_0$	none	flat	$[-1, 1]$
$\tilde{\beta}_\infty$	none	flat	$[-1, 1]$
$\log_{10} r_t$	pc	flat	$[0, 2]$
η	none	flat	$[0, 4]$
r_{cen}	pc	flat	$[0.5, 2.5]$
$\log_{10} M_{\text{cen}}$	M_\odot	flat	$[0, 6]$
$\log_{10} M_{\text{BH}}$	M_\odot	flat	$[0, 6]$
$\log_{10} M_\star$	M_\odot	flat	$[5, 8]$
$\log_{10} M_p$	M_\odot	flat	$[0, 6]$
α	none	flat	$[-8, -2]$
r_0	pc	flat	$[0, 10]$
$\log_{10} B_i$	G	normal	$\mu = 8.47$ $\sigma = 0.33$
l	4.54 pc	flat	$[-10, 10]$

Notes. To ensure a broad range of values is considered, the variable $\log_{10} B_i$ [G] is sampled over the flat range $[6, 10]$, inside which the normal prior is applied. See discussion in text for more details on the priors adopted.

5.3. Full likelihood and priors

The full log-likelihood can now be summarized as

$$\begin{aligned} \ln \mathcal{L}_{\text{tot}}(\theta) &= \ln \mathcal{L}_{\text{LOS}} + \ln \mathcal{L}_{\text{PM,t}} + \ln \mathcal{L}_{\text{PM,R}} + \ln \mathcal{L}_{\text{VSP1}} \\ &+ \ln \mathcal{L}_{\text{VSP2}} + \ln \mathcal{L}_{p, \text{LOS}} + \ln \mathcal{L}_{\text{pos}} + \ln \mathcal{L}_{\text{pos, R}}, \end{aligned} \quad (39)$$

where θ includes all the model parameters which are simultaneously fitted, including anisotropy, photometric profile, MSP distribution, and mass model parameters. This is an important aspect of this study, as it allows for a fully consistent statistical treatment of the data and exploring potential degeneracies and correlations between different parameters, such as the aforementioned mass-anisotropy degeneracy. This interdependence of parameters may not otherwise be evident if one were to make separate fits or fix some of these parameters implicitly. Importantly,

as will be shown in subsequent sections, it also allows for a full exploitation of the constraints imposed by the data in a way that differs from the results obtained from a separate treatment.

The prior on l is expressed in terms of the core-radius length scale $r_c \equiv 4.54$ pc of Baumgardt & Hilker (2018), which is also used by Dai et al. (2023). Following Read & Steger (2017), we also work with the symmetrized anisotropy:

$$\tilde{\beta} \equiv \frac{\beta}{2 - \beta} \quad (40)$$

for $-1 \leq \tilde{\beta} \leq 1$ to efficiently sample the (infinitely) broad range of possible values of β .

Table 2 shows the priors we use in our analysis, whose results will be discussed in the subsequent sections. The prior on α is based on the range of physically expected limits for pulsar populations, following the discussion in Phinney (1993); Prager et al. (2017).⁸ These limits are chosen to be broad and away from the tails of the posterior distribution in most cases, so that results are insensitive to them, while being sufficiently narrow to allow for satisfactory numerical efficiency. Priors in log-space are designed to efficiently span a broad range of several orders of magnitude.

The fits are performed using the nested sampling package *dynesty* (Speagle 2020; Koposov et al. 2022). This is based on nested sampling techniques (Skilling 2004, 2006) and the subsequently developed dynamic nested sampling technique (Higson et al. 2019), which we use, and is optimized for the inference of posterior distributions (as opposed to evidence estimation), using the bounding method from Feroz et al. (2009). The sampling method used is based on Neal (2003); Handley et al. (2015a,b). These methods are designed for more efficient sampling of complex posterior distributions which may present multimodalities and a potentially large number of dimensions in parameter space. The reason for this choice is that, in these settings, traditional Markov-chain Monte Carlo techniques tend to have less satisfactory performance, with numerical convergence being harder to achieve and the process being costly in CPU time. Another advantage of *dynesty* is that it is comparatively simple to implement, with the inclusion of an automated initialization routine and stopping criteria.⁹

6. Kinematic fits and constraints on a central mass

Fig. 1 summarizes the fitting results obtained for the stellar kinematics and photometry observables used for the analysis. For the LOS and PM velocity dispersions and the two virial shape parameters, we obtain a best-fit reduced chi-square value of $\chi^2_v = 1.61$ for our 4-parameter anisotropy profile and a 3-parameter mass model (stellar mass and Plummer mass and scale radius). Note that we have excluded both the black hole and MSP profile components due to the fact they do not have relevant kinematic contributions in our fits and adding them does not materially improve them.¹⁰ This is consistent with our finding that

⁸ We found that extending these limits within the physically allowable range that allows for convergence and positivity of the distribution does not greatly affect its overall shape due to the degeneracy in the parameters r_0 and α .

⁹ For further information, see:

<https://dynesty.readthedocs.io/en/latest/index.html>.

¹⁰ More precisely, the introduction of MSP and IMBH components leads to a higher χ^2_v value, due to the introduction of 4 additional parameters and a negligible effect on the total chi-square statistic, showing no statistically significant preference for these two components based on the additional degrees of freedom that they introduce.

the data strongly favor an extended central mass in the inner regions and a stellar/photometric component in the outer ones, while excluding at 3σ CL an IMBH greater than $6 \times 10^3 M_\odot$, or a kinematically relevant distribution of intermediate concentration traced by the MSPs. This bound on a putative IMBH mass is significantly more constraining than those reported in previous analyses. This result is illustrated in Fig. 2, which shows the posterior distributions of the mass model parameters and the mass and anisotropy profiles.

One reason for our bound being comparatively stringent is due to the extended central distribution that is favored, limiting the kinematic contribution of additional central components. This result was found to be statistically significant, since the $\sim 10^4 M_\odot$ and $\sim 10^5 M_\odot$ total mass values required for kinematically significant IMBH and MSP profile contributions (respectively) exceed the 3σ limits of our derived posterior distributions, and are thus self-consistently excluded by the fit. We also found that, when fitting only the MSP component to model extended remnants, the MSP distribution was forced to emulate the concentration of our central mass favored by the kinematics, but failed to reproduce the more extended distribution of the MSPs, which is implicitly accounted for in the position likelihood components. This can be seen when comparing the cumulative distribution functions of the various components, which are examined in Sec. 7 (Fig. 4). This result indicates the need for a more concentrated mass component that is distinct from one traced by the pulsars.

Our results show a clear preference for a two-component model with an extended central mass of $\sim 2 - 3 \times 10^5 M_\odot$ and scale radius between 1.5 and 2.2 pc at the 3σ level. This is favored over an IMBH, leading to a 3σ upper bound of $6 \times 10^3 M_\odot$ and placing a coexistence region for a putative IMBH of at most a few thousand solar masses. Our analysis also places a 3σ upper bound for the MSP distribution of $6 \times 10^4 M_\odot$, strongly limiting the kinematic contribution of the more extended MSP component.¹¹

This is not present in previous analyses by construction, since these fit a single component of either a point mass or an extended distribution accounting for remnants, but not both simultaneously.¹² While previous studies have indicated the kinematic degeneracy between extended central distributions and an IMBH, in our analysis we are able to consider them simultaneously in a self-consistent fit.

One way the stellar kinematics favor this result is by having velocity dispersion profiles that are relatively flat in the central regions, with a value of $\lesssim 20$ km/s within the inner ~ 0.1 pc, while still being sufficiently elevated within a few pc from the center to favor a significant extended central mass component of $\sim 2 - 3 \times 10^5 M_\odot$ that is needed in addition to the photometric

¹¹ This result can be more dependent on the modeling of the other extended components in the distribution, especially if these exhibit degeneracies with each other. However, this is not the case in our analysis, as a kinematically relevant contribution is disfavored for this component. Further, we found that the precise values the 3σ bounds in this study can show moderate stochastic variability when comparing multiple independent runs of the fits, while this has only a moderate effect (agreeing at the specified number of significant figures in most cases), we chose the cited values conservatively so that they exclude at least at the 3σ level, across the multiple (more than 10) runs considered.

¹² Note also that while a single-component Plummer sphere or a similar extended mass model can in principle accommodate for a point mass in the limit of vanishing scale radius, it suffers the limitation of being a mutually exclusive model in that it does not explore the coexistence between a point mass and an extended one.

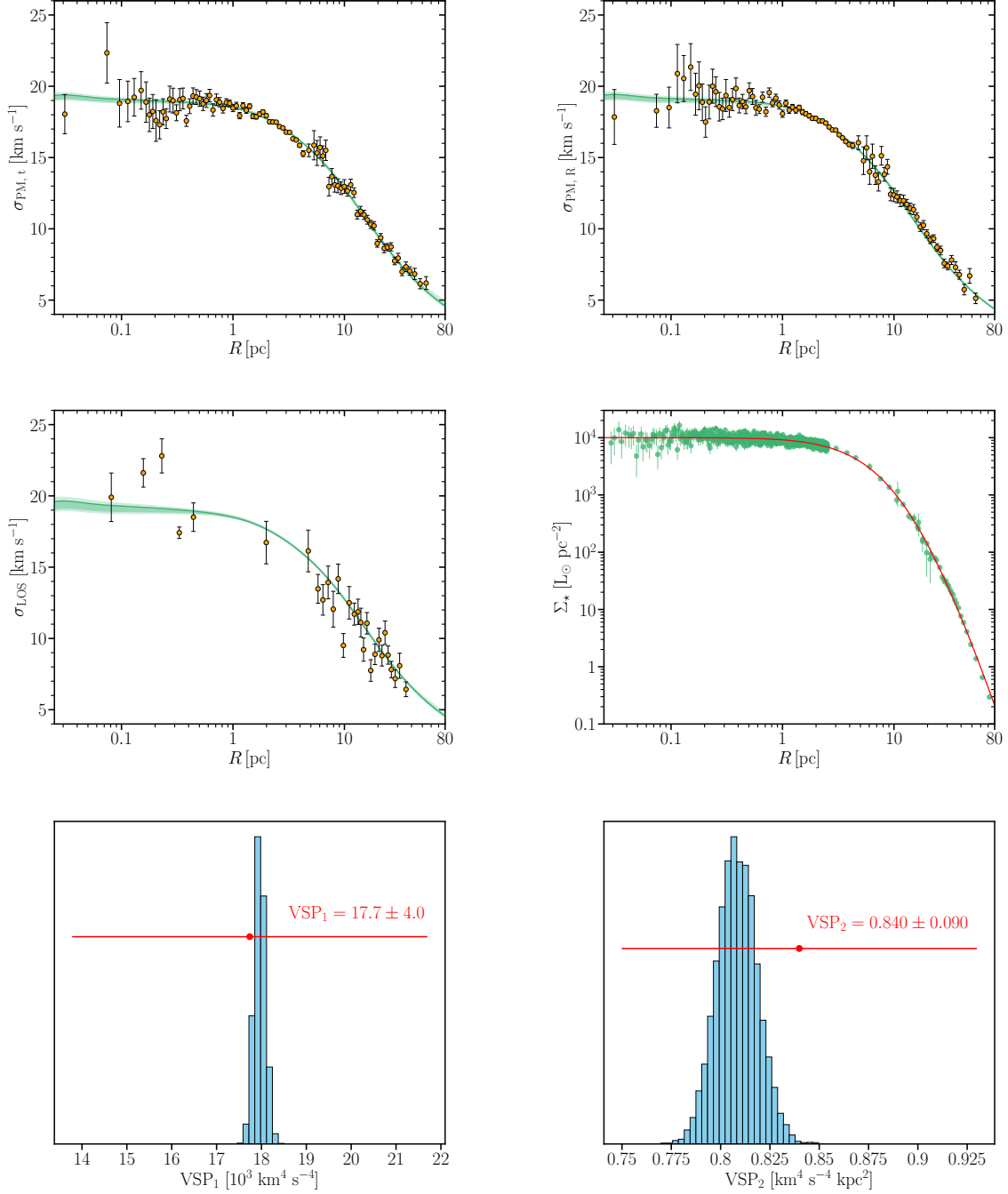


Fig. 1. Fits to stellar kinematic observables and the photometric light profile. The profiles are a function of projected radius at the assumed distance of 5.2 kpc. The green lines and bands correspond to the maximum posterior values, and the 68% and 95% CL centered at the median (respectively). The proper motion data are a combination of the HST and Gaia datasets reported in Bellini et al. (2017) and Vasiliev & Baumgardt (2021) respectively, while the LOS data are compiled from Reijns et al. (2006); Noyola et al. (2010); Kamann et al. (2018) (see Sec. 3). All data, including the photometric profile, have been self-consistently binned with the center from Anderson & Van der Marel (2010). Upper left: Tangential proper motion velocity dispersion. Upper right: Radial proper motion velocity dispersion. Middle left: LOS velocity dispersion. Middle right: Surface brightness profile used to determine the photometric component of the distribution. The red line shows the best-fit profile that was used throughout the analysis (see Sec. 2 for details). Lower left: Posterior distribution for the virial shape parameter 1 as a result of the fits, with the red data point indicating the value with 1σ errors computed by binulator (see Sec. 3). Lower right: The same as the lower left figure, but for the virial shape parameter 2.

one. Large ($\geq 10^4 M_{\odot}$) IMBH models predict distinct cusps in velocity dispersion profiles (cf. Figure 5 of Zocchi et al. (2019)), while more extended distributions do not. The fact that no such cusp is observed in our data, which has sufficient resolution to probe this central region, disfavors the presence of such compo-

nent, and is instead consistent with the flatter profile predicted by the extended central mass component.

The similarity between the three velocity dispersion components explored is a manifestation of the approximate isotropy of the distribution, leading to a relatively well-constrained

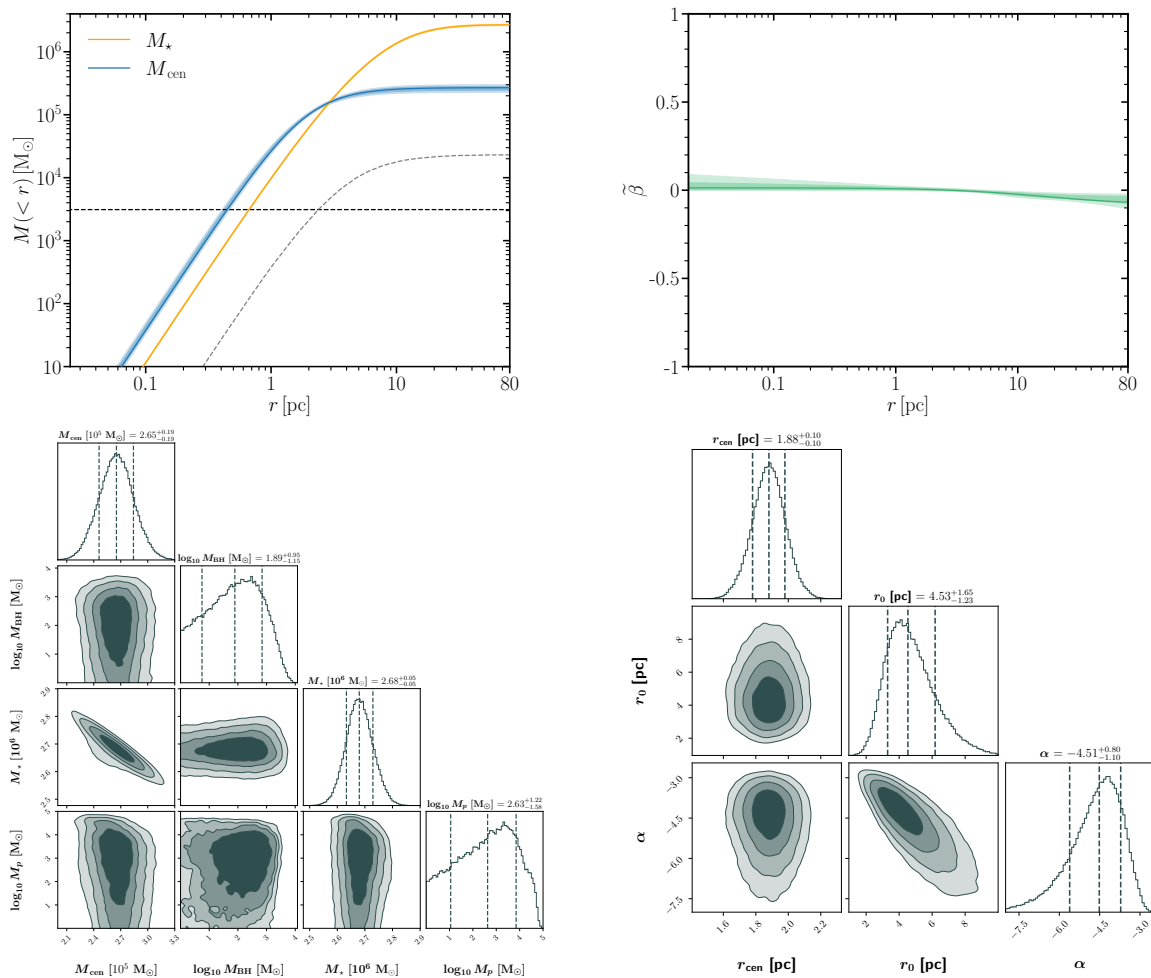


Fig. 2. Upper left: 3D enclosed mass profile including photometric, central remnants, black hole, and MSP mass components. The solid lines correspond to the maximum posterior with 68% and 95% CL regions. The black and gray dashed lines indicate the upper limit of the 95% CL region for the black hole and MSP components, respectively. Upper right: Symmetrized anisotropy profile including the maximum posterior and 68% and 95% CL regions. The posterior distributions for the anisotropy parameters are presented in Appendix A. The profile is close to isotropic, with a mild radial (tangential) anisotropy in the inner (outer) regions. This translates to the 1σ CL band being well within $|\bar{\beta}| < 0.1$, or $|\beta| \lesssim 0.15$ for the vast majority of the range covered. Lower left: Posterior distributions for the masses of the various fitted components of our analysis, indicating the median and 68% CL region at the top of each distribution. Lower right: Posterior distributions for the morphological parameters of the fitted mass profiles with respective median and 68% CL regions.

anisotropy profile. This can be observed clearly in Fig. C.2, where the three velocity dispersion components are plotted in the same figure, and is also apparent from the (symmetrized) anisotropy profile in Fig. 2.

The dynamical mass of the photometric component yields $M_{\star} = 2.68 \pm 0.05 \times 10^6 M_{\odot}$, which for a total luminosity of $\sim 1.25 \times 10^6 L_{\odot}$ would imply a mass-to-light ratio that is comparable, but arguably higher than those typical of stellar populations, showing consistency with previous studies, with some suggesting ω Cen to have high remnant fractions, for instance, in the form of white dwarfs (Dickson et al. 2024). For the photometric profile in Fig. 1 (middle right), we found this to be very well constrained by the data in morphology via the surface brightness data, yielding a very good fit with $\chi^2_{\nu} = 1.13$ for the 4-parameter model used. This, in addition to previous runs we performed where we fitted it with the kinematic data, justifies the simpler approach to fix the profile to its best-fit values.

Fig. 3 illustrates the fits to the MSP kinematics corresponding to the LOS acceleration profiles for pulsars for the 5 MSPs

with suitable timing solutions, noting that for the 13 remaining ones only projected positions were used as a constraint on the MSP distribution profile. We may now ask, more generally, the degree to which the MSP data are constraining of the overall mass distribution in this analysis. An important result in this regard is that our self-consistent fit with the MSP data yields a central mass component that is systematically more extended and massive when MSP accelerations are included, with an increase of $\sim 20\%$ in both the mass and scale radius of the distribution, with the black-hole and photometric components being comparatively unaffected (cf. Appendix B, where a fit is performed without including MSP accelerations).

The dominant contribution to this effect appears to be attributable to the most distant MSP acceleration data point, which effectively sets a lower limit on the enclosed mass at that point. The other data points were found to be independently consistent with the remaining pulsars, including the innermost one, whose relatively high acceleration was found to be potentially conflicting by Dai et al. (2023) with the models they explored, as these

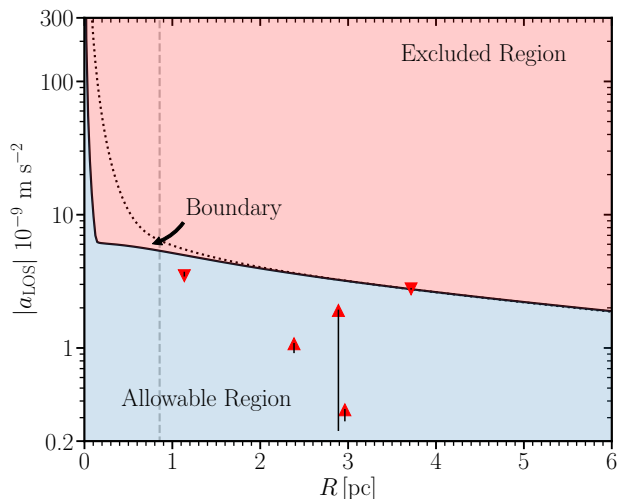


Fig. 3. Absolute values of MSP LOS accelerations. The black, solid line denotes the 95%CL upper bounds as inferred from the mass profiles of the posterior distribution. This region marks the boundary between the excluded region (red) and the allowable one (blue), where it is possible to find a value of l (i.e. a position within the cluster) compatible with the LOS acceleration at a given projected radius. The upwards (downwards) pointing triangles denote the observed MSP accelerations with positive (negative) values, as inferred from the MSP timing data. Errors are not included as they fall below the size of the data points. The vertical black lines denote the intrinsic spin-down components leading to the intrinsic LOS accelerations that trace the GC potential, based on the 68% CL regions in the magnetic field strength posteriors. This interval accounts for 84% of the posterior distribution as it includes the lower tail below the 16% percentile value in addition to the 68% CL interval contributions. The black, dotted line shows the corresponding bound for an illustrative model where $\sim 15\%$ of the central mass distribution is concentrated in the form of a $4 \times 10^4 M_{\odot}$ IMBH. As can be seen, this model is still consistent with the pulsar accelerations (triangles), but is in tension with the proper motion and line of sight velocity data. A lower mass IMBH is still allowed (see the central allowable region that reaches to higher accelerations). The gray, dashed line indicates the projected position of the innermost detected MSP in ω Cen at ~ 0.86 pc from its center.

do not account for the presence of an inner dark mass such as the one favored in our analysis. Dai et al. (2023) also indicated a potential tension with this outermost point during their analysis. However, the degree to which such a tension is present in our analysis is necessarily dependent on the assumptions made on the intrinsic spin-down component, due to the fact that the lower bound implied by the observed apparent acceleration is within the allowable region of our analysis. While this data point favors a low intrinsic spin-down component, we found it to agree at the 2σ level with the observationally derived prior on the magnetic field strength parameter, with the other MSPs agreeing at the 1σ level. Considering also the significant observational and modeling uncertainties inherent to intrinsic spin-down determinations, we do not consider this to imply a significant tension in our analysis. It is interesting to note, however, that the constraining power effected by the outermost data point is robust with respect to intrinsic spin-down effects, as higher negative contributions to the acceleration would only increase the degree to which a more massive and extended distribution is favored.

In summary, we find the tension examined by Dai et al. (2023) to be alleviated by this analysis as a result of including a central dark mass component in our model which emulates an

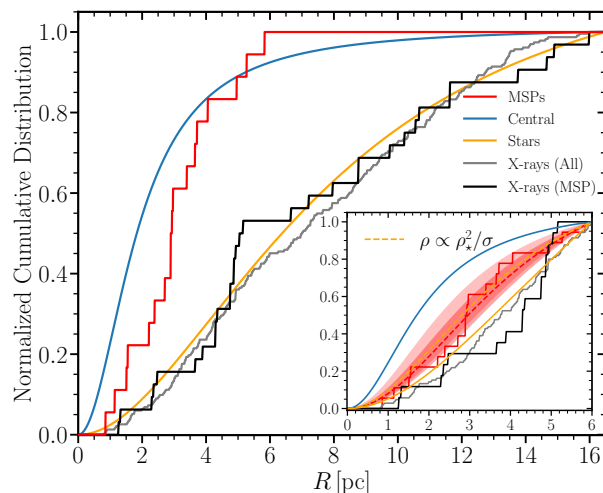


Fig. 4. Normalized cumulative distributions of MSPs (red), the more concentrated central mass emulating heavier stellar remnants (blue), stars (yellow) and X-ray emitting sources (black and gray) in ω Cen as a function of projected radius. The inset shows a close-up view of the distribution normalized at a smaller radius, where all of the 18 MSPs are located. The inset includes the 68% and 95% CL regions of the MSP profile fit (shaded bands). The red dashed line denotes the median of the inferred cumulative distribution from the MSP 3D density from Eq. (30). The dashed-orange line indicates the predicted distribution derived from the stellar encounter rate that provides a remarkable match to the MSP distribution. We also show counts of X-ray sources observed in ω Cen studied by Henleywillis et al. (2018), showing the total count of 233 objects (black) and a subset of ~ 32 of the objects that share luminosities and X-ray colors compatible with known MSPs from other GCs (gray), as presented in Figure 10 of Heinke et al. (2005) (see also the discussion in Henleywillis et al. (2018)). Over the radial range of the inset figure, this count is reduced to 105 and ~ 17 sources, respectively.

extended cluster of stellar remnants (see discussion in Sec. 8.2), and by our statistical treatment of intrinsic spin-down modeling which allows quantifying the significance of putative tensions.

For illustrative purposes, we also show in Fig. 3 the effect of concentrating $\sim 15\%$ of the central mass component in the form of a $4 \times 10^4 M_{\odot}$ IMBH, which is representative of some of the values in the literature (Noyola et al. 2008; Baumgardt 2017). We observe that, while in both models extremal LOS accelerations are allowable, the larger IMBH model would produce significant extremal accelerations over a larger region within the inner ~ 0.5 pc, comparable to the radius of the circle of influence of the putative IMBH. A detection of such an extremal acceleration within this region would constitute a ‘smoking-gun’ signature of such an IMBH. Such scenario is disfavored by stellar kinematics in our analysis, except for the very inner region within $\lesssim 0.1$ pc, where a smaller IMBH of at most a few thousand solar masses is still allowable. This limited presence of extremal accelerations remains a falsifiable prediction in the context of our analysis, should new MSPs be detected in the innermost regions of ω Cen (cf. gray, dashed line of Fig. 3).

7. Analysis of the pulsar distribution

Fig. 4 shows the (normalized) cumulative distributions of the MSP, photometric, and extended central mass components derived from our model fits. We also plot an independent dataset of

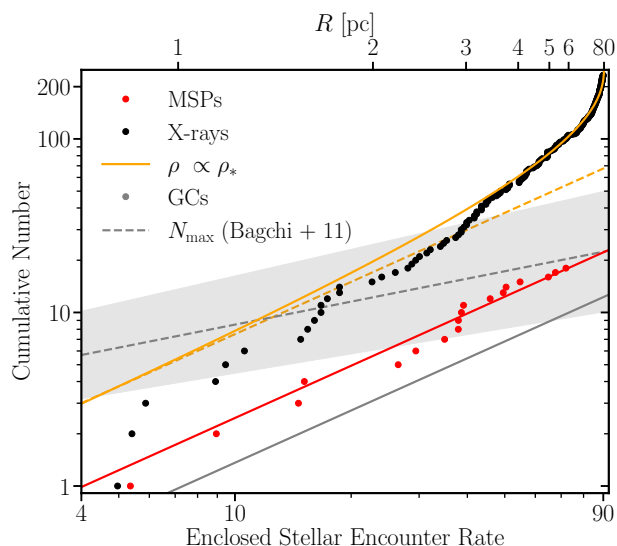


Fig. 5. MSP abundances as a function of stellar encounter rates. The red points are the observed cumulative number of MSPs as a function of the enclosed encounter rate at a projected radius R (upper x-axis). The red line corresponds to a least-squares linear fit, showing a clear linear dependence. The black points denote the same quantities for the full list of 233 X-ray sources from Henleywillis et al. (2018), while the orange line corresponds to the stellar distribution, normalized to match these sources. These show a distinct, non-linear, dependence, with encounter rates that are not followed by the MSPs. The orange, dashed line is a linear extrapolation shown for comparison. Lastly, the gray dashed line indicates an upper estimate on the total number of MSPs as a function of total encounter rates of GCs, with 1σ error bands. This is based on the parametric fit performed by Zhao & Heinke (2022) using the phenomenological estimates of Bagchi et al. (2011), based on luminosity functions, and assuming the updated total stellar encounter rates of Bahramian et al. (2013). Units for ω Cen’s total encounter have been normalized to match the 90.4 central value of Bahramian et al. (2013).

X-ray sources shown for comparison purposes. The morphology of the MSP distribution is well constrained by the MSP data. It is clear from the figure that the MSP distribution is significantly more concentrated than the photometric component. The X-ray dataset was introduced to compare whether it may be independently traced by the components explored in this study. This is of particular interest given that 11 of the 18 known MSPs in ω Cen possess X-ray counterparts (Zhao & Heinke 2023; Dai et al. 2023). While it seems highly plausible that some of the MSPs are in fact found among these X-ray sources, interestingly, we find that the aggregate distribution of X-ray sources appears to be traced by the (more extended) stellar density profile, which, as implied by our previous discussion, was determined independently from stellar photometric data. This result appears to be essentially independent of which of the two X-ray sources is included, with the one sharing MSP-like properties (black) matching the total distribution (gray).

We now consider what the more concentrated MSP profile that we find here can tell us about MSP formation. MSPs have long been thought to descend from low mass X-ray binaries (e.g. see Bahramian et al. (2013); Verbunt & Freire (2014)). These form dynamically in GCs at a rate set, to leading order, by the rate of stellar encounters.¹³ Such models predict that the abundance of MSPs in GCs should scale with the (total) stellar en-

¹³ This may also apply more generally to comparable models involving formation via two-body encounters that are not limited to low mass X-ray binaries.

counter rate for the cluster $\Gamma \propto \int dr r^2 \rho_*(r)^2 / \sigma(r)$, where $\rho_*(r)$ is the 3D density profile of stars, $\sigma(r)$ is the 3D velocity dispersion profile of the stars, with $\rho_*(r)^2 / \sigma(r)$ being the encounter rate density, which encapsulates the rate of two-body stellar interactions (hence the ρ_*^2) and is enhanced by gravitational focusing (hence the inverse relation to σ). In practice, however, we may expect some deviation from this relation as the formation of MSPs depends on the binary stellar encounter rate that can differ from the single-star one (e.g. Verbunt & Freire 2014), binary population statistics, loss of stars from the cluster (impacted by the cluster escape velocity; Yin et al. 2024), neutron star retention fractions (e.g. Verbunt & Freire (2014)), and the effects of mass segregation (e.g. see Bahramian et al. (2013) and references therein). Despite these caveats, numerous studies have reported a correlation between the MSP population abundances and the (total) stellar encounter rate in GCs (Bahramian et al. 2013; Zhao & Heinke 2022).

Previous studies have focused on establishing correlations between total encounter rates and abundances of MSPs in GCs. Following the above discussion, we decided to extend these analyses by assessing whether a similar relation exists at the intra-cluster level. In particular, we explore whether the MSP population density scales with the stellar encounter rate density so that $\rho_p(r) \propto \rho_*(r)^2 / \sigma(r)$, which would naturally predict a linear correlation with the total encounter rate when both of these quantities are integrated over the volume of the cluster.

In the inset panel of Fig. 4, we compare our derived radial density profile of MSPs (shaded bands) with a model in which the MSP distribution depends solely on the stellar encounter rate (yellow dashed line). This gives an excellent match. Indeed, if we perform an indicative fit of the form $\rho_p(r) \propto \rho_*(r)^\gamma / \sigma(r)$, we find that $\gamma = 1.9 \pm 0.3$, showing excellent agreement for the central value of the inferred MSP distribution and well within its 68% CL bounds. Since we found that $\sigma(r) \propto \rho_*(r)^{0.2}$ to a good approximation for the region covered by the inset, this relation can also be expressed directly in terms of the stellar distribution as $\rho_p(r) \propto \rho_*(r)^{1.7}$ for the central values.

Fig. 5 shows explicitly the dependence of the distributions considered as a function of the encounter rates, which for the case of ω Cen can be mapped to the profile via the enclosed encounter rate over a cylindrical volume with projected radius R , which we define as:

$$\Gamma(< R) \propto \int_{-\infty}^{\infty} dl \int_0^R dR' R' \rho_*(r)^2 / \sigma(r), \quad (41)$$

where $r = \sqrt{R'^2 + l^2}$.

Encounter rates are usually expressed in arbitrary units, which in our case have adapted to be consistent with Bahramian et al. (2013) for the total value (i.e. $\Gamma(< \infty) \sim 90.4$). For obtaining the constant of proportionality K mapping the encounter rate to the number of MSPs, we perform a least-squares fit (Fig. 5: red line) where we model the cumulative number of MSPs as:

$$\text{Number of MSPs}(< R) = K \Gamma(< R), \quad (42)$$

yielding $K \sim 0.25$. This closely matches the central value of the total number of MSPs (~ 23) independently predicted by the phenomenological relation from Zhao & Heinke (2022) (Fig. 5: gray, dashed line). However, the 1σ upper bound of this relation implies more than double the abundance, suggesting that ω Cen could host a significant number of yet-undiscovered MSPs. One can also use the kinematic component of the MSP distribution to derive a strict upper bound on the MSP abundance assuming

the totality of the dynamical mass being due to $\sim 1.6 M_{\odot}$ MSP binary systems, obtaining $\sim 4 \times 10^4$ at 3σ CL (c.f. Fig. 2).

The most significant result from Fig. 5 is the clear linear scaling observed for the MSP distribution, yielding a relation analogous to those from previous works for total encounter rates and abundances of GCs, but for the enclosed intra-cluster populations instead. This validates the model from Eq. (42), showing excellent consistency with the expectation from stellar encounter models of MSP formation discussed earlier.

On the other hand, for the case of the stellar density profile and the X-ray sources independently traced by it, we observe markedly different behavior, with a distinct non-linear dependence followed in both cases. This further illustrates the differences between these distributions, with the linear scaling behavior being a unique characteristic of the MSP population.

To the knowledge of the authors, while such scaling relations have been explored at the level of total encounter rates and MSP counts for GC populations, this constitutes the first analysis where a similar relationship is validated as a function of radius within a single GC, thus motivating a functional form for the profile of the pulsar distribution within the cluster.

It is also interesting to note that, following the discussion of Sec. 8.2, since significant mass segregation for lighter stellar remnants (which MSPs are part of) is not expected for ω Cen, a different mechanism would be needed to explain their more concentrated distribution. This further validates the stellar encounter model, which naturally predicts the rate of encounters to be proportional to the square of the stellar density, and thus leads to a more concentrated distribution. This consideration, in conjunction with its abundance of recently discovered pulsars, makes ω Cen an ideal candidate to study such models of MSP formation.¹⁴

8. Discussion

8.1. Method

The conflicting results in the literature regarding the nature of a central dark mass component in ω Cen are likely attributable to systematic differences in the data considered and the mass-anisotropy modeling adopted. For instance, Noyola et al. (2008) only considered a limited dataset of radial velocities for the stellar kinematics, while also assuming isotropy, which can lead to degenerate effects with anisotropic mass components (e.g. Zocchi et al. (2017); Read & Steger (2017)). As noted in Sec. 8.2, degenerate effects with central remnants should also be accounted when considering the potential presence of IMBHs. These aspects have been extensively addressed in our analysis, with the inclusion of flexible mass-anisotropy modeling and a full self-consistent consideration multiple stellar kinematic data, including also MSP accelerations as an additional constraint.

Noyola et al. (2010) found a dependence of the inferred central mass with the assumed location of the kinematic center in their analysis, with the center used in Anderson & Van der Marel (2010) leading to a lower estimate of the inferred central mass. In a recent study from Pechetti et al. (2024), employing 3 independent center determinations, it was concluded that the favored center led to inferred stellar kinematics determinations that were consistent with the results from different datasets across multiple studies, including those of Anderson & Van der Marel (2010)

using HST data. However, a significant tension was found with the originally assumed center in Noyola et al. (2008). This is also consistent with the findings of Anderson & Van der Marel (2010), where the Noyola et al. (2008) center was ruled out at high confidence and determined to be susceptible to systematic errors not originally considered in the study of Noyola et al. (2008).

We have addressed this issue using data with self-consistent centers (including our derived binning) for the kinematics and photometry, while also considering different centers such as the ones from Noyola et al. (2010) and Noyola et al. (2008). These results are shown in Appendix C (Figs. C.1 and C.2). While the inferred velocity dispersion profiles appear broadly consistent with those derived with the Anderson & Van der Marel (2010) center, we found that the central mass component derived with this center has a median mass (scale radius) that is $\sim 15\%$ ($\sim 11\%$) lower using the Noyola et al. (2010) center and $\sim 14\%$ ($\sim 10\%$) higher using the Noyola et al. (2008) center, with less significant effects on the remainder of the mass components in both cases. This indicates a somewhat more extended inferred central mass distribution when using the Noyola et al. (2010) center and a more concentrated one for the Noyola et al. (2008) center. This shows that the essential conclusions of our analysis are robust with respect to the choice of centers considered, with the main effect being a moderate variability in the concentration of the central mass component.

Another aspect in the literature concerns the various cluster distances adopted. We note that the close-to-isotropic distribution which is apparent in the data (cf. Figs. 2 and C.2) shows independent consistency with the 5.2 kpc adopted. This was further validated by performing a fit in which the distance was varied, showing a strong preference for the value adopted. This is not a trivial result given the different distance dependencies of PM and LOS velocity components and adds further support to the distance determinations in Watkins et al. (2015b), which exploit this effect. This value also shows agreement with the distance determinations of the Harris (1996) catalog (2010 edition) and the more recent ones from Baumgardt & Vasiliev (2021).

Another factor which may play a role in central mass determinations as seen, for instance, in Anderson & Van der Marel (2010), would be the photometric profile determinations. These authors found that different assumptions about the morphology of the photometric component led to differences in the degree to which central masses were favored. This is indicative of the importance of using a photometric profile which accurately reproduces the photometry. In this regard, the introduction of the $\alpha\beta\gamma$ profile as applied to this study, which was found to produce excellent fits to the photometry, constitutes a significant methodological improvement with respect to other modeling approaches which may nonetheless work well for other cases.¹⁵

8.2. A dark cluster of remnants in ω Cen

It is apparent from our results in Sec. 6 that the two kinematically relevant components, namely, the extended central mass and photometric profiles, are very well constrained by the data. In this context, it is instructive to compare our results with the analyses of Zocchi et al. (2019); Baumgardt et al. (2019); Dickson et al. (2024), where the presence of a cluster of stellar-mass black holes is determined to be a viable alternative to the IMBH

¹⁴ Cf. Chen et al. (2023), where the idealness of ω Cen for probing the MSP distribution based on its lack of mass segregation was also independently argued as a promising direction for future studies.

¹⁵ One such example we considered was a generic three-component Plummer model, which we found to produce significantly inferior fits to the photometry, despite having a larger number of free parameters.

hypothesis to account for the observed velocity dispersions in ω Cen. Stellar-mass black holes also arise naturally in dynamical simulations, where they have been found to play an important role in the core dynamics of GC analogs, and are predicted to be hosted in significant numbers by many present-day GCs (Kremer et al. 2020). Indeed, a concentrated cluster of remnants appears to be the only viable interpretation for the dominant mass component favored for the central region that our analysis favors over any of the other mass components considered. A two-component model of light and heavier remnants as the kinematically relevant contributions is indeed favored by our model, in agreement with the theoretically motivated assumptions of these studies.

Dickson et al. (2024) performed a recent analysis of ω Cen among other GCs, in which Limpey distribution function models (Gieles & Zocchi 2015) were used to obtain realistic distributions for an ample spectrum of species comprising stellar-mass black holes, white dwarfs, neutron stars and main sequence stars. These were subsequently fitted to velocity dispersion and stellar mass function data following the procedure described in Dickson et al. (2023). A key finding from this study is the presence of a substantial central mass component dominated by stellar-mass black holes, with total mass $1.82^{+0.05}_{-0.06} \times 10^5 M_{\odot}$, while the remaining lighter remnants follow the same profile to a good approximation. This favors a two-component mass model whereby the segregation of lighter objects is inhibited. This shows broad agreement with previous studies of ω Cen where this has been argued, owing to its young dynamical age, long two-body relaxation time, and black hole population abundance, which has been found to be anti-correlated with mass segregation (Dickson et al. 2024). We were able to explicitly compare our results with the projected mass profiles from Dickson et al. (2024). We found that for the region beyond ~ 1 pc, the profile from (Dickson et al. 2024) closely matched a Plummer sphere with scale radius ~ 1.5 pc,¹⁶ compared to our derived value of 1.88 ± 0.10 pc. While this implies a profile that is systematically more concentrated than the one we derive, it agrees at the $\sim 1\sigma$ level with the $\sim 20\%$ less massive and extended profile we obtained without the inclusion of MSP accelerations. This result is shown in Appendix B (Figs. B.1 and B.2), where a fit without the inclusion of MSP accelerations is performed for comparison. Interestingly, this suggests the analysis of Dickson et al. (2024) may benefit from the inclusion of MSP accelerations following our implementation, leading to a profile that would likely be more consistent with the one we obtain. Notwithstanding systematic uncertainties due to modeling assumptions, which should be fully accounted for a more definitive comparison, the similarity of these profiles, and the fact that lighter remnants would not be able to undergo the degree of segregation implied by our derived central mass distribution, stellar-mass black holes indeed appear to be the favored interpretation for our derived central component.

8.3. An IMBH in ω Cen?

Häberle et al. (2024) recently derived a lower bound on the mass of an IMBH in ω Cen of $8.2 \times 10^3 M_{\odot}$ based on the observation of centrally located fast-moving stars, in apparent tension with our

¹⁶ We note that, while the modeling of Dickson et al. (2024) indicates a more concentrated distribution for the remnants below this radius which is not reproduced by the Plummer model, our inclusion of a point mass has the ability to compensate for this should a higher enclosed mass be favored for this region. The fact that it does not do so at a statistically significant level indicates that such feature, while physically expected from the remnant models of Dickson et al. (2024), is likely not relevant for the kinematics considered in our analysis.

3σ bound of $6 \times 10^3 M_{\odot}$. However, this bound is dependent on the assumed escape velocity for the cluster, which, for instance, is $\sim 10\%$ higher in our analysis due to the presence of an extended dark mass attributable to stellar remnants (see Sec. 8.2).

Pechetti et al. (2024), on the other hand, found no evidence of an IMBH in the form of fast-moving stars in the inner ~ 0.5 pc region predicted by N-body IMBH simulations from Baumgardt (2017). Baumgardt et al. (2019) arrived at a similar conclusion based on the lack of observed fast-moving stars in their analysis, concluding that a $\sim 4 \times 10^4 M_{\odot}$ IMBH, favored by other analyses (Noyola et al. 2008; Baumgardt 2017), is ruled out in favor of a cluster of remnants, which is consistent with our results.

IMBH formation simulations in clusters have also found it challenging to produce black holes exceeding $\sim 500 M_{\odot}$ due to the ejection from gravitational wave recoils in black hole merger interactions (Arca Sedda et al. 2023; Fujii et al. 2024). Interestingly, in recent simulations from Fujii et al. (2024), it was found to be possible to produce $\gtrsim 10^3 M_{\odot}$ IMBHs in GC analogs via very-massive star formation processes. However, the authors conclude that this formation scenario disallows IMBHs of masses greater than $10^4 M_{\odot}$, even for the case of very massive GCs such as ω Cen. This poses a theoretical challenge for any claims of IMBH detections in GCs exceeding this limit.

Many works have suggested that ω Cen is the stripped remnant of a nucleated dwarf (Bekki & Freeman 2003; Wirth et al. 2020; Johnson et al. 2020; Gray et al. 2024). If so, it should have a dark matter halo and a correspondingly higher escape velocity. This could explain the fast-moving stars found in Häberle et al. (2024) without the need for such a massive IMBH, or also the observation from Pechetti et al. (2024) of a fast-moving star with a high (0.99) cluster membership probability that appears too distant from the center ($\gtrsim 1.5$ pc) to be accounted for by an IMBH. We will test this idea quantitatively in forthcoming papers in which we will add a dark matter halo to our ω Cen models.

9. Conclusion

The results and main findings of this work can be summarized as follows:

- We performed a combined analysis of stellar kinematics and LOS accelerations of MSPs to probe the mass contents of ω Cen. We explored the existence of a central dark mass component and considered competing interpretations of its nature: a cluster of stellar remnants or an IMBH. We also exploited the data to model and constrain the MSP distribution, using this to probe MSP formation models, and as an additional mass component in the model that traces stellar remnants of intermediate mass.
- There are two key results from our analysis which are not present in previous works: One is that a two-component model with a significantly extended central mass distribution (with scale radius between 1.5 and 2.2 pc at the 3σ level) is strongly favored over both an IMBH (or more concentrated distributions) and the more extended component traced by the MSPs. The other result, which is a consequence of the previous one, is that we arrive at stringent bounds on the kinematic contributions of the two additional components considered, establishing a coexistence region between the favored central mass distribution and a putative IMBH with a $6 \times 10^3 M_{\odot}$ 3σ CL upper limit on its mass. This altogether favors a dark cluster of remnants, rather than an IMBH, as

the explanation for the central kinematics of ω Cen.

- While the MSP profile, with a 3σ CL upper bound of $5 \times 10^4 M_{\odot}$, was found not to contribute meaningfully to the dynamical mass distribution of ω Cen, we found that the MSP timing constraints do play a significant role in the kinematics, favoring a central distribution that is $\sim 20\%$ more massive and extended.

- We found that the MSP density profile goes as:

$$\rho_p(r) \propto \rho_{\star}(r)^{\gamma} / \sigma(r),$$

with $\gamma = 1.9 \pm 0.3$, consistent with models in which MSPs originate from stellar encounters. It is a natural expectation from this scenario that $\gamma \sim 2$. We found, further, that the stars and X-ray sources in ω Cen are more radially extended than the MSPs and follow a similar density profile to one another. Our analysis leads to a significant novelty: that the encounter rate-MSP abundance correlation can be extended at the intra-cluster level, motivating a profile for the spatial distribution of these objects.

- In future work, we will explore the presence of a dark matter halo in our mass model, as is predicted to be present if ω Cen is the dissolved remnant of an accreted, nucleated, dwarf (e.g. Gray et al. 2024).
- Despite limited observations leading to full timing solutions for only 5 of the 18 recently discovered MSPs in ω Cen, and more potential discoveries still underway (Chen et al. 2023), our analysis shows the potential and promise of combining velocity dispersion data with pulsar accelerations to probe the inner mass distribution of GCs. Future observations may allow probing whether extremal accelerations occur for central MSPs, a ‘smoking-gun’ signature of an IMBH and a disfavored scenario for ω Cen in our analysis.
- With the number of MSP discoveries in GCs having recently doubled over a 5-year period amid the advent of radio surveys with unprecedented sensitivity, such as MeerKAT, FAST, and notably the upcoming SKA, it is foreseeable that the methodology we introduce will be increasingly relevant for the understanding of the kinematics of these systems.

References

- Abbate, F., Possenti, A., Colpi, M., & Spera, M. 2019, *ApJ*, 884, L9
- Abbate, F., Possenti, A., Ridolfi, A., et al. 2018, *Mon. Not. Roy. Astron. Soc.*, 481, 627
- Anderson, J. & Van der Marel, R. P. 2010, *The Astrophysical Journal*, 710, 1032
- Anderson, S. B. 1993, *A study of recycled pulsars in globular clusters* (California Institute of Technology)
- Arca Sedda, M., Kamlah, A. W. H., Spurzem, R., et al. 2023, *MNRAS*, 526, 429
- Baes, M. & van Hese, E. 2007, *A&A*, 471, 419
- Bagchi, M., Lorimer, D. R., & Chennamangalam, J. 2011, *MNRAS*, 418, 477
- Bahramian, A., Heinke, C. O., Sivakoff, G. R., & Gladstone, J. C. 2013, *ApJ*, 766, 136
- Battaglia, G., Helmi, A., & Breddels, M. 2013, *New Astronomy Reviews*, 57, 52
- Baumgardt, H. 2017, *MNRAS*, 464, 2174
- Baumgardt, H., He, C., Sweet, S. M., et al. 2019, *Monthly Notices of the Royal Astronomical Society*, 488, 5340
- Baumgardt, H. & Hilker, M. 2018, *Monthly Notices of the Royal Astronomical Society*, 478, 1520
- Baumgardt, H. & Vasiliev, E. 2021, *MNRAS*, 505, 5957
- Bekki, K. & Freeman, K. C. 2003, *Mon. Not. Roy. Astron. Soc.*, 346, L11
- Bellini, A., Anderson, J., Bedin, L. R., et al. 2017, *ApJ*, 842, 6
- Bellini, A., Anderson, J., van der Marel, R. P., et al. 2014, *ApJ*, 797, 115
- Binney, J. & Mamon, G. A. 1982, *MNRAS*, 200, 361
- Binney, J. & Tremaine, S. 2008, *Galactic Dynamics: Second Edition*
- Brown, A. M., Massey, R., Lacroix, T., et al. 2019 [arXiv:1907.08564]
- Chen, W. et al. 2023, *Mon. Not. Roy. Astron. Soc.*, 520, 3847
- Chon, S. & Omukai, K. 2020, *MNRAS*, 494, 2851
- Collins, M. L. M., Read, J. I., Ibata, R. A., et al. 2021, *MNRAS*, 505, 5686
- Dai, S., Johnston, S., Kerr, M., et al. 2023, *Mon. Not. Roy. Astron. Soc.*, 521, 2616
- Dai, S., Johnston, S., Kerr, M., et al. 2020, *Astrophys. J. Lett.*, 888, L18
- de Boer, T. J. L., Gieles, M., Balbinot, E., et al. 2019, *MNRAS*, 485, 4906
- de Lorenzi, F., Gerhard, O., Coccato, L., et al. 2009, *MNRAS*, 395, 76
- Di Cintio, A., Brook, C. B., Dutton, A. A., et al. 2014, *MNRAS*, 441, 2986
- Dickson, N., Hénault-Brunet, V., Baumgardt, H., Gieles, M., & Smith, P. J. 2023, *MNRAS*, 522, 5320
- Dickson, N., Smith, P. J., Hénault-Brunet, V., Gieles, M., & Baumgardt, H. 2024, *MNRAS*, 529, 331
- Dinescu, D. I., Girard, T. M., & van Altena, W. F. 1999, *AJ*, 117, 1792
- Evans, A. J., Strigari, L. E., & Zivick, P. 2022, *Mon. Not. Roy. Astron. Soc.*, 511, 4251
- Feroz, F., Hobson, M. P., & Bridges, M. 2009, *MNRAS*, 398, 1601
- Freire, P. C. C. et al. 2017, *Mon. Not. Roy. Astron. Soc.*, 471, 857
- Freundlich, J., Jiang, F., Dekel, A., et al. 2020, *MNRAS*, 499, 2912
- Fujii, M. S., Wang, L., Tanikawa, A., Hirai, Y., & Saitoh, T. R. 2024, arXiv e-prints, arXiv:2406.06772
- Genina, A., Read, J. I., Frenk, C. S., et al. 2020, *MNRAS*, 498, 144
- Gieles, M. & Zocchi, A. 2015, *MNRAS*, 454, 576
- Gray, E. I., Read, J. I., Taylor, E., et al. 2024, arXiv e-prints, arXiv:2405.19286
- Grindlay, J. E., Camilo, F., Heinke, C. O., et al. 2002, *Astrophys. J.*, 581, 470
- Handley, W. J., Hobson, M. P., & Lasenby, A. N. 2015a, *MNRAS*, 450, L61
- Handley, W. J., Hobson, M. P., & Lasenby, A. N. 2015b, *MNRAS*, 453, 4384
- Harris, W. E. 1996, *AJ*, 112, 1487
- Heinke, C. O., Grindlay, J. E., Edmonds, P. D., et al. 2005, *ApJ*, 625, 796
- Helmi, A., Van Leeuwen, F., McMillan, P., et al. 2018, *Astronomy & astrophysics*, 616, A12
- Hénault-Brunet, V., Gieles, M., Strader, J., et al. 2020, *MNRAS*, 491, 113
- Henleywillis, S., Cool, A. M., Haggard, D., et al. 2018, *MNRAS*, 479, 2834
- Hernquist, L. 1990, *ApJ*, 356, 359
- Higson, E., Handley, W., Hobson, M., & Lasenby, A. 2019, *Statistics and Computing*, 29, 891
- Häberle, M., Neumayer, N., Seth, A., et al. 2024, *Fast-moving stars around an intermediate-mass black hole in Omega Centauri*
- Ibata, R. A., Bellazzini, M., Malhan, K., Martin, N., & Bianchini, P. 2019, *Nature Astronomy*, 3, 667
- Jalali, B., Baumgardt, H., Kissler-Patig, M., et al. 2012, *Astronomy & Astrophysics*, 538, A19
- Jeans, J. H. 1922, *MNRAS*, 82, 122
- Johnson, C. I., Dupree, A. K., Mateo, M., et al. 2020, *The Astronomical Journal*, 159, 254
- Júlio, M. P., Brinchmann, J., Zoutendijk, S. L., et al. 2023 [arXiv:2307.13035]
- Kamann, S., Husser, T. O., Dreizler, S., et al. 2018, *MNRAS*, 473, 5591
- Kızıltan, B., Baumgardt, H., & Loeb, A. 2017a, *Nature*, 542, 203
- Kızıltan, B., Baumgardt, H., & Loeb, A. 2017b, *Nature*, 545, 510
- Koposov, S., Speagle, J., Barbary, K., et al. 2022, *joshspeagle/dynesty: v1.2.3*
- Kremer, K., Ye, C. S., Chatterjee, S., Rodriguez, C. L., & Rasio, F. A. 2020, in *Star Clusters: From the Milky Way to the Early Universe*, ed. A. Bragaglia, M. Davies, A. Sills, & E. Vesperini, Vol. 351, 357–366
- Lokas, E. L. & Mamon, G. A. 2003, *MNRAS*, 343, 401
- Lugger, P. M., Cohn, H. N., & Grindlay, J. E. 1995, *ApJ*, 439, 191
- Mamon, G. A. & Lokas, E. L. 2005, *MNRAS*, 363, 705
- Manchester, R. N., Hobbs, G. B., Teoh, A., & Hobbs, M. 2005, *VizieR Online Data Catalog*, VII/245
- Massari, D., Koppelman, H. H., & Helmi, A. 2019, *Astronomy & Astrophysics*, 630, L4
- Merrifield, M. R. & Kent, S. M. 1990, *AJ*, 99, 1548
- Merritt, D. 1985, *MNRAS*, 214, 25P
- Myeong, G., Vasiliev, E., Iorio, G., Evans, N., & Belokurov, V. 2019, *Monthly Notices of the Royal Astronomical Society*, 488, 1235
- Neal, R. M. 2003, *The Annals of Statistics*, 31, 705
- Nice, D. J. & Taylor, J. H. 1995, *ApJ*, 441, 429
- Noyola, E., Gebhardt, K., & Bergmann, M. 2008, *Astrophys. J.*, 676, 1008
- Noyola, E., Gebhardt, K., Kissler-Patig, M., et al. 2010, *ApJ*, 719, L60
- Osipkov, L. P. 1979, *Pisma v Astronomicheskii Zhurnal*, 5, 77
- Padmanabh, P. V., Ransom, S. M., Freire, P. C. C., et al. 2024, arXiv e-prints, arXiv:2403.17799
- Pechetti, R., Kamann, S., Krajnović, D., et al. 2024, *MNRAS*, 528, 4941
- Perera, B. B. P., Stappers, B. W., Lyne, A. G., et al. 2017a, *MNRAS*, 471, 1258
- Perera, B. B. P., Stappers, B. W., Lyne, A. G., et al. 2017b, *Mon. Not. Roy. Astron. Soc.*, 468, 2114
- Phinney, E. S. 1993, in *Astronomical Society of the Pacific Conference Series*, Vol. 50, *Structure and Dynamics of Globular Clusters*, ed. S. G. Djorgovski & G. Meylan, 141

- Plummer, H. C. 1911, *MNRAS*, 71, 460
- Portegies Zwart, S. F., Baumgardt, H., Hut, P., Makino, J., & McMillan, S. L. W. 2004, *Nature*, 428, 724
- Prager, B. J., Ransom, S. M., Freire, P. C. C., et al. 2017, *Astrophys. J.*, 845, 148
- Read, J. I. & Steger, P. 2017, *MNRAS*, 471, 4541
- Read, J. I., Walker, M. G., & Steger, P. 2018, *MNRAS*, 481, 860
- Reid, M. J., Menten, K. M., Brunthaler, A., et al. 2014, *ApJ*, 783, 130
- Reijns, R. A., Seitzer, P., Arnold, R., et al. 2006, *A&A*, 445, 503
- Reynoso-Cordova, J., Burgueño, O., Geringer-Sameth, A., et al. 2021, *JCAP*, 02, 010
- Richardson, T. & Fairbairn, M. 2014, *MNRAS*, 441, 1584
- Ridolfi, A., Gautam, T., Freire, P. C. C., et al. 2021, *MNRAS*, 504, 1407
- Shklovskii, I. 1970, *Soviet Astronomy*, Vol. 13, p. 562, 13, 562
- Skilling, J. 2004, in *American Institute of Physics Conference Series*, Vol. 735, *Bayesian Inference and Maximum Entropy Methods in Science and Engineering: 24th International Workshop on Bayesian Inference and Maximum Entropy Methods in Science and Engineering*, ed. R. Fischer, R. Preuss, & U. V. Toussaint, 395–405
- Skilling, J. 2006, *Bayesian Analysis*, 1, 833
- Smith, P. J., Hénault-Brunet, V., Dickson, N., Gieles, M., & Baumgardt, H. 2024, arXiv e-prints, arXiv:2407.06274
- Sollima, A., Bellazzini, M., Smart, R. L., et al. 2009, *MNRAS*, 396, 2183
- Speagle, J. S. 2020, *MNRAS*, 493, 3132
- Strigari, L. E., Bullock, J. S., & Kaplinghat, M. 2007, *ApJ*, 657, L1
- van de Ven, G., van den Bosch, R. C. E., Verolme, E. K., & de Zeeuw, P. T. 2006, *A&A*, 445, 513
- van der Marel, R. P. 1994, *MNRAS*, 270, 271
- Van der Marel, R. P. & Anderson, J. 2010, *The Astrophysical Journal*, 710, 1063
- Vasiliev, E. & Baumgardt, H. 2021, *MNRAS*, 505, 5978
- Verbunt, F. & Freire, P. C. C. 2014, *A&A*, 561, A11
- Vleeschower, L., Corongiu, A., Stappers, B. W., et al. 2024, *MNRAS*[arXiv:2403.12137]
- Wang, L.-C. & Xie, Y. 2021, *Research in Astronomy and Astrophysics*, 21, 270
- Watkins, L. L., van de Ven, G., den Brok, M., & van den Bosch, R. C. E. 2013, *MNRAS*, 436, 2598
- Watkins, L. L., van der Marel, R. P., Bellini, A., & Anderson, J. 2015a, *ApJ*, 803, 29
- Watkins, L. L., van der Marel, R. P., Bellini, A., & Anderson, J. 2015b, *ApJ*, 812, 149
- Wilkinson, M. I., Kleyna, J., Evans, N. W., & Gilmore, G. 2002, *Mon. Not. Roy. Astron. Soc.*, 330, 778
- Wirth, H., Bekki, K., & Hayashi, K. 2020, *Monthly Notices of the Royal Astronomical Society: Letters*, 496, L70
- Xie, Y. & Wang, L.-C. 2020, *Research in Astronomy and Astrophysics*, 20, 191
- Xie, Y., Yin, D., Wang, L., et al. 2024, *MNRAS*, 527, 7743
- Yin, D., Zhang, L.-y., Qian, L., et al. 2024, arXiv e-prints, arXiv:2405.18228
- Zentner, A., Dandavate, S., Slone, O., & Lisanti, M. 2022, *JCAP*, 07, 031
- Zhang, L., Freire, P. C. C., Ridolfi, A., et al. 2023, *ApJS*, 269, 56
- Zhao, H. 1996, *MNRAS*, 278, 488
- Zhao, J. & Heinke, C. O. 2022, *MNRAS*, 511, 5964
- Zhao, J. & Heinke, C. O. 2023, *MNRAS*, 526, 2736
- Zocchi, A., Gieles, M., & Hénault-Brunet, V. 2017, *MNRAS*, 468, 4429
- Zocchi, A., Gieles, M., & Hénault-Brunet, V. 2019, *MNRAS*, 482, 4713

10. Acknowledgements

We are grateful to Renuka Pechetti for kindly providing us the photometric data used in this work. We would like to thank Vincent Hénault-Brunet, Giuseppina Battaglia, José María Arroyo Polonio, Paul Beck, Addy J. Evans, Jorge Sánchez Almeida, Claire S. Ye, and P.C.C. Freire for instructive discussions and their interest in our work. We also thank Joshua S. Speagle for providing us valuable information about the use of *dynesty*. We are grateful to Jorge Terol Calvo, Jorge García Farieta, and Ángel de Vicente for the invaluable support provided in using the high-performance computing systems at Instituto de Astrofísica de Canarias (IAC). We are grateful to Elena Pinetti and the team at the Cosmic Physics Center at Fermilab, including Alex Drlica-Wagner and Albert Stebbins, where this work was presented and discussed. The authors wish to acknowledge the contribution of the IAC High-Performance Computing support team and hardware facilities to the results of this research. AB and JMC acknowledge support from the MICINN through the grant “Dark-Maps” PID2022-142142NB-I00. JIR would like to acknowledge support from STFC grants ST/Y002865/1 and ST/Y002857/1.

Appendix A: Posterior distributions of the anisotropy parameters

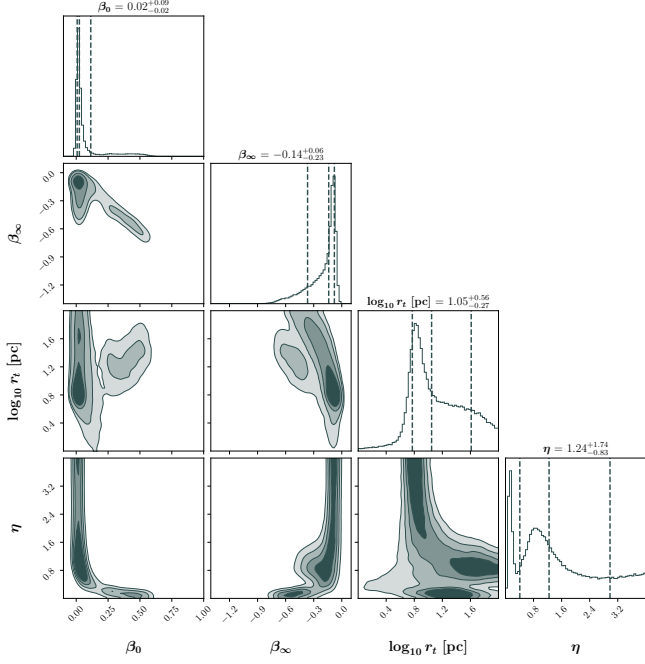


Fig. A.1. Posterior distributions of the anisotropy parameters. The parameter space exhibits multiple degeneracies, but due to the correlations inherent to these, the resultant anisotropy profile is well constrained (cf. Fig. 2). Note that this is not inconsistent with our results and that these degeneracies are the result of our parametric modeling and not intrinsic to the anisotropy profile.

Appendix B: Effects of excluding MSP accelerations

Appendix C: Use of different centers

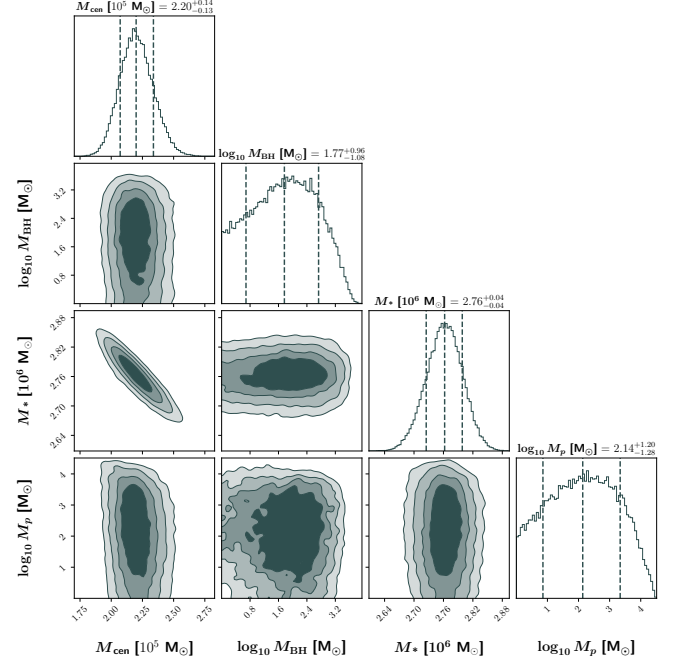


Fig. B.1. Posterior distributions for the masses of the components considered during a fit performed without the inclusion of MSP LOS accelerations into the likelihood function. The median for the central mass from the full fit (cf. Fig. 2) is $\sim 20\%$ greater than the one found during this fit, with the other components showing only moderate differences.

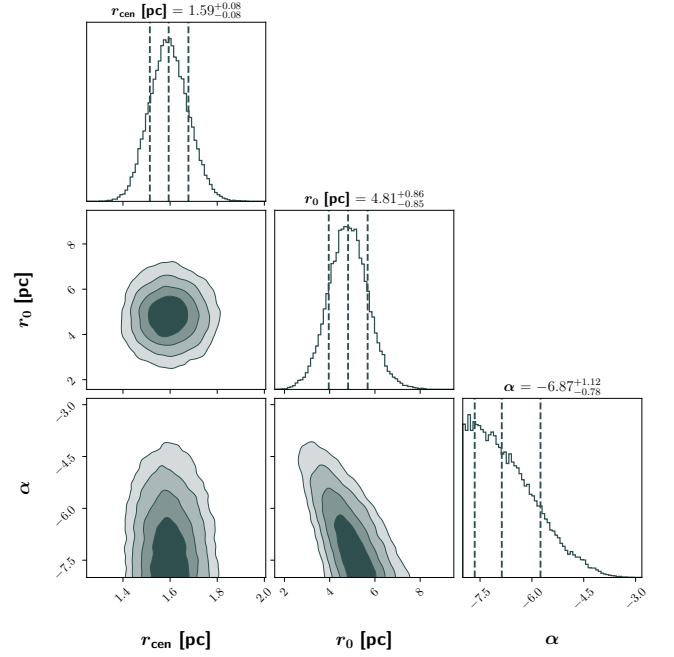


Fig. B.2. Posterior distributions for the morphological parameters of the mass profiles without the inclusion of MSP LOS accelerations into the likelihood function. The median for the central mass length scale from the full fit (cf. Fig. 2) is $\sim 18\%$ greater than the one found during this fit. The morphology of the MSP distribution is still constrained due to the projected radii included in the positional component of the likelihood function, favoring a somewhat different posterior distribution when accelerations are excluded. This, however, has a negligible effect on the remainder of the mass components in the absence of accelerations to constrain their kinematics.

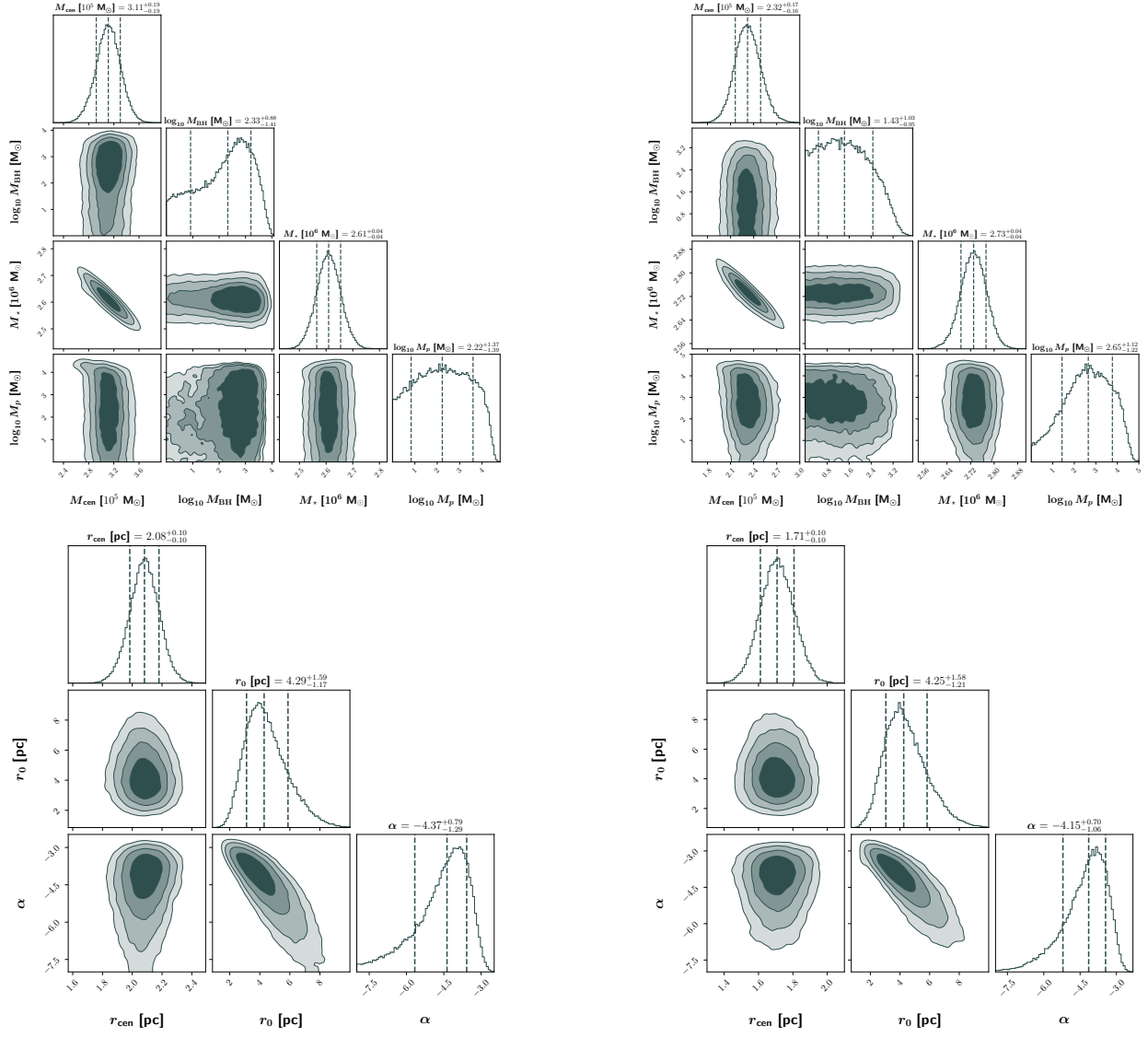


Fig. C.1. Upper-left: Posterior distributions for the mass components considered in our kinematic models using the Noy10 center. The median of the central mass component for the And center, is $\sim 15\%$ lower, consistent with a more extended central mass distribution for the Noy10 center. The stellar mass obtained is only marginally smaller ($\lesssim 3\%$), with the other IMBH and MSP components remaining subdominant without significant statistically meaningful differences. Upper-right: Same as the upper-left plot, but for the Noy08 center. In this case, the central mass for our main analysis with the And center is $\sim 14\%$ higher than the result shown, consistent with a more concentrated distribution for the Noy08 center, although still with the 1σ CL regions overlapping each other. A small increase of $\lesssim 2\%$ is observed with respect to the stellar mass value, but these central values lie within their respective 1σ CL regions. The IMBH and MSP mass components, once more, show approximate consistency with the previous results.† Lower-left: Posterior distributions of the morphological parameters for the mass models using the Noy10 center. The median of the scale radius using the And center is $\sim 11\%$ lower, indicating a somewhat more extended central mass distribution for the Noy10 center, with the 1σ CL regions barely overlapping each other. The MSP parameters agree at the 1σ level. Lower-right: Same as the middle-left plot, but for the Noy08 center. In this case, the median of the scale radius using the And center is $\sim 10\%$ greater, indicating a somewhat more concentrated central mass distribution, but still showing 1σ CL compatibility. As with the Noy10 center, the MSP parameters show 1σ level consistency with the And center results.

† Marginal differences in the morphology of the posterior distributions of the IMBH and MSP masses are not necessarily statistically meaningful, owing to the fact that, due to being inherently less constrained, these may require additional independent runs to fully establish such differences (which we did perform for the case of the And center). This, however, is not necessary for the purposes of the complementary analysis presented in this appendix.

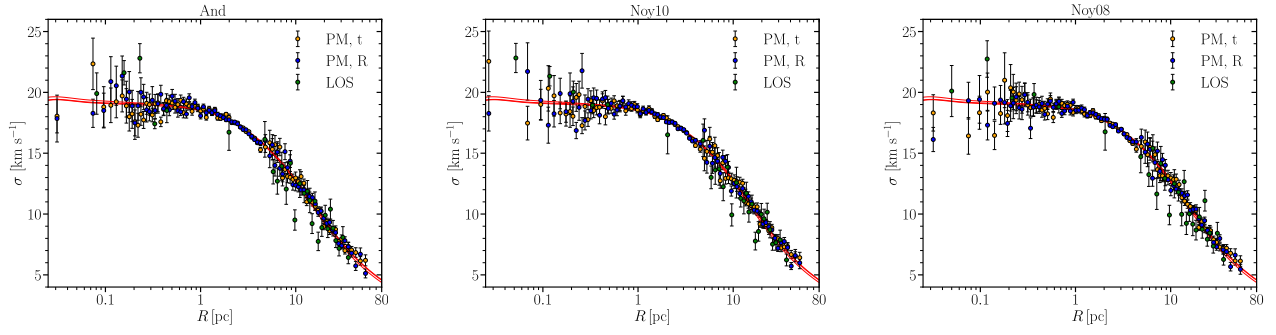


Fig. C.2. Combined velocity dispersion profiles for the three components using the [Anderson & Van der Marel \(2010\)](#) center (And, left) [Noyola et al. \(2010\)](#) (Noy10, middle) and [Noyola et al. \(2008\)](#) (Noy08, right) kinematic centers. The maximum-posterior velocity dispersion profile (red) from our main analysis using the And center is shown for reference in all plots, yielding fits of comparable quality for all the cases considered. Due to the close-to-isotropic behavior of our inferred distribution at the 5.2 kpc distance employed, the three components of our maximum posterior fits are almost identical, with the large majority of the data points showing close overlap with each other.